

RESEARCH ARTICLE

10.1029/2017JB015214

Key Points:

- We use poroelasticity and chemical mass balance to derive a model of fluid flow, elastic deformation, and mass transfer in porous media
- We derive a parametrization of surface energy effects and demonstrate its ability to drive fluid flow into low-permeability rock
- Using a model of serpentinization in a subseafloor environment we predict that reaction-driven volume changes can lead to tensile failure

Correspondence to:

O. Evans,
ore2000@columbia.edu

Citation:

Evans, O., Spiegelman, M., & Kelemen, P. B. (2018). A poroelastic model of serpentinization: Exploring the interplay between rheology, surface energy, reaction, and fluid flow. *Journal of Geophysical Research: Solid Earth*, 123, 8653–8675. <https://doi.org/10.1029/2017JB015214>

Received 10 NOV 2017

Accepted 5 OCT 2018

Accepted article online 11 OCT 2018

Published online 29 OCT 2018

A Poroelastic Model of Serpentinization: Exploring the Interplay Between Rheology, Surface Energy, Reaction, and Fluid Flow

Owen Evans¹ , Marc Spiegelman^{1,2,3} , and Peter B. Kelemen^{2,3}

¹Department of Applied Physics and Applied Mathematics, Columbia University, New York, NY, USA, ²Lamont-Doherty Earth Observatory, Columbia University, Palisades, NY, USA, ³Department of Earth and Environmental Sciences, Columbia University, New York, NY, USA

Abstract The interactions between reactive fluids and solids are critical in Earth dynamics. Implications of such processes are wide ranging: from earthquake physics to geologic carbon sequestration and the cycling of fluids and volatiles through subduction zones. Peridotite alteration is a common feature in many of these processes, which—despite its obvious importance—is relatively poorly understood from a geodynamical perspective. In particular, although frequently observed in nature, it is still unknown how rocks can undergo 100% hydration/carbonation. One potential explanation of this observation is the mechanism of *reaction-driven cracking*: that volume changes associated with these reactions are large enough to fracture the surrounding rock, leading to a positive feedback where new reactive surfaces are exposed and fluid pathways are created. The purpose of this study is to investigate the relative roles of reaction, elastic stresses, and surface tension in alteration reactions. In this regard, we derive a system of equations describing reactive fluid flow in elastically deformable porous media, which we apply to a model of serpentinization in a subseafloor environment. The stoichiometry of the serpentinization reaction predicts net volume reduction of the multiphase system, which, according to our numerical simulations, can lead to failure in tension. We also explore a parameterization of surface energy in the model, which allows fluid to infiltrate regions of dry peridotite, significantly changing the stresses and potentially leading to growing crack fronts.

1. Introduction

The interaction of reactive fluids and solids in regions of the Earth's outer brittle shell is important in many geodynamic processes. This covers a broad range of the Earth's activity, from chemical weathering at the Earth's surface to the global carbon cycle, supporting chemosynthetic microbial habitats, water cycling through subduction zones, and geologic carbon sequestration. Specific examples of processes where reactive-brittle dynamics may play a critical role include alteration during hydrothermal circulation and cooling at oceanic spreading centers (Craft & Lowell, 2009), the transport of volatiles from the subducting lithosphere to the mantle wedge source of arc magmas (Gorman et al., 2006), alteration resulting from bending-related faulting at subduction zones (Ranero et al., 2003), sustaining alteration along oceanic transform faults (Roland et al., 2010), the transformation of bedrock to saprolite by spheroidal weathering (Fletcher et al., 2006); and dehydration/decarbonation reactions in the subducting mantle and crust, which may have implications for intermediate-depth earthquakes (Kirby et al., 1996) and fluid transport (Wilson et al., 2014).

Peridotite alteration—which includes both hydration and carbonation reactions—is a common feature in many of these processes. Mantle peridotite is thermodynamically unstable at near-surface conditions and therefore tends to react rapidly with the atmosphere and surface waters when it is unearthed from the depths (Malvoisin et al., 2012; Martin & Fyfe, 1970). In regions where mantle peridotite is exposed, for example, the Samail ophiolite in the Sultanate of Oman, carbonate veins formed during peridotite alteration have an average ¹⁴C age of ≈26,000 years (Chavagnac, Ceuleneer, et al., 2013; Chavagnac, Monnin, et al., 2013; Kelemen & Matter, 2008; Kelemen et al., 2011; Mervine et al., 2013). Thus, the process of alteration in the Samail ophiolite is still happening to this day, in keeping with similar processes elsewhere (e.g., California, Barnes & O'Neil, 1969; Italy, Bruni et al., 2002; New Caledonia, Barnes et al., 1978), where it is estimated that 10⁴–10⁵ tonnes of CO₂ are being consumed per year. In light of this observation, it has been proposed that the process of natural

olivine carbonation could be exploited as a means of storing large amounts of CO₂ (Kelemen & Matter, 2008; Kelemen et al., 2011).

The current understanding of the alteration process is limited, however, and there is particular uncertainty regarding the feedbacks between mineral reactions and fluid transport. For one thing, observations of 100% hydrated peridotites (serpentinites) and carbonated peridotites (listvenites) appear to contradict the idea that fluid-rock reactions involving an increase in solid volume are self-limiting (e.g., Aharonov et al., 1998; Ten-thorey et al., 1998). This *self-limiting* behavior can be attributed to several negative feedbacks, one example being that hydration/carbonation reactions can result in a net solid volume increase. This may reduce the permeability, limiting the remaining fluid from accessing unreacted areas of the solid. Another important negative feedback could be armoring of reactive surfaces by newly formed reaction products—for example, serpentine or carbonate minerals—so that continued reaction is limited by slow diffusion.

There are two main theories that have been offered to explain how 100% hydration/carbonation can occur in spite of these negative feedbacks. The first is that replacement reactions occur at constant volume; that is, the increase in solid volume is offset by the dissolution/export of chemicals back into the fluid (Fletcher & Merino, 2001). However, analysis of serpentinites and listvenites suggests that aside from the addition of water into the peridotite, the formation process occurs under isochemical conditions (i.e., the bulk composition of the rock remains largely unchanged) (Coleman & Keith, 1971; Falk & Kelemen, 2015; Kelemen et al., 2017). The second theory proposes that elastic stresses associated with large volume changes during reaction are sufficient to fracture the host rock (Macdonald & Fyfe, 1985). The generation of fractures may introduce a positive feedback where fluid pathways are created and new reactive surfaces are exposed, thus allowing the reaction to go until completion. This so-called *reaction-driven cracking* has motivated several recent studies of peridotite serpentinization and carbonation (Iyer et al., 2008; Jamtveit et al., 2008, 2011; Kelemen & Hirth, 2012; Kelemen & Matter, 2008; Kelemen et al., 2011; Malvoisin et al., 2017; Plümper et al., 2012; Rudge et al., 2010; Ulven, Jamtveit, & Malthe-Sørenssen, 2014; Ulven, Storheim, et al., 2014; Zhu et al., 2016).

To understand the basic feedbacks in peridotite alteration, we use a model that aims to capture the essential chemistry and physics of this process. This model is an extension of Biot's equations of poroelasticity (Biot, 1941) that includes reaction between fluid/solid phases and surface energy effects. The derivation of the model is based closely on the theory of magma transport in viscously deformable mantle rock, which is a macroscopic description of mass, momentum, and energy conservation that was originally developed by McKenzie and others in the 1980s (Fowler, 1985; McKenzie, 1984; Scott & Stevenson, 1986) and later extended by others (e.g., Bercovici & Ricard, 2003; Bercovici et al., 2001a, 2001b; Katz et al., 2006; Katz, 2008; Keller et al., 2013; Rudge et al., 2011; Scott & Stevenson, 1989; Spiegelman, 1993a, 1993b; Spiegelman et al., 2001). To address the problem of fluid migration into regions of low permeability, we consider the potential for fluid flow driven by gradients in surface energy; this has been examined by others in the context of melt/fluid migration in partially molten rock (Bercovici & Ricard, 2003; Bercovici et al., 2001a, 2001b; Hier-Majumder et al., 2006; Stevenson, 1986).

The structure of the paper is as follows. Section 2 details the model derivation. Section 3 discusses the constitutive choices. In Section 4 we nondimensionalize the system of equations and interpret the resulting dimensionless parameters. In section 5 we outline the geometrical setup of the model, the boundary/initial conditions and discuss the ranges of parameters relevant to serpentinization of peridotite in a subseafloor setting. The results of the numerical simulations are presented and analyzed in section 6, which is broken down into three subsections that discuss (i) the fundamental behavior of the model (in the absence of surface energy), (ii) how the behavior of the model varies over the space of parameters and initial conditions, and (iii) the behavior when surface energy is included. Further discussion of the implications of these results and limitations of the model is provided in section 7, and a summary of the key conclusions is stated in section 8. Details of the numerical implementation are provided in Appendix B.

2. Governing Equations

2.1. Conservation of Mass

In this section we derive mass conservation equations for a general hydration reaction of the form



where H₂O is water, *A* is the (immobile) solid reactant, and *B* is the solid product. Treating each of these

constituents as a separate phase leads to the following mass conservation statements:

$$\frac{\partial}{\partial t}(\rho_f \phi_f) + \nabla \cdot [\rho_f \phi_f \mathbf{v}_f] = v_f R, \quad (2)$$

$$\frac{\partial}{\partial t}(\rho_A \phi_A) + \nabla \cdot [\rho_A \phi_A \mathbf{v}_A] = v_A R, \quad (3)$$

$$\frac{\partial}{\partial t}(\rho_B \phi_B) + \nabla \cdot [\rho_B \phi_B \mathbf{v}_B] = v_B R, \quad (4)$$

where ϕ_i is the volume fraction of phase i , ρ_i is the density, \mathbf{v}_i is the velocity, v_i is related to the stoichiometric coefficients for the reaction (see below), and R is the mass transfer rate of the full reaction (units: $\text{kg} \cdot \text{m}^{-3} \cdot \text{s}^{-1}$). From this point on we will use ϕ in place of ϕ_f to represent the fluid phase fraction (i.e., the porosity). It should also be noted that ϕ is always the porosity under fully fluid saturated conditions.

Equations (2)–(4) are also subject to the following constraints:

$$\phi + \phi_A + \phi_B = 1, \quad (5)$$

$$\rho_A \phi_A + \rho_B \phi_B = \rho_s (1 - \phi), \quad (6)$$

where ρ_s is the density of the composite solid. The stoichiometric coefficients as written in equations (2)–(4) represent concentrations (in weight percent) of each of the components in the reaction. By convention, stoichiometric coefficients are negative for reactants and positive for products. If m_i denotes the molar mass of phase i , then the stoichiometric coefficients can be written as

$$v_f = -\frac{m_f}{m_B}, \quad v_A = -\frac{m_A}{m_B}, \quad v_B = 1, \quad (7)$$

where $m_A + m_f = m_B$ must hold (De Groot & Mazur, 1962).

We assume that the solid phase is mechanically homogeneous—meaning that we can introduce a single solid velocity \mathbf{v}_s —and that ρ_A and ρ_B may be treated as constants. These two assumptions allow us to rewrite (3) as

$$\frac{D_s \phi_A}{Dt} = -\phi_A \nabla \cdot \mathbf{v}_s + \frac{v_A}{\rho_A} R. \quad (8)$$

These two assumptions in conjunction with equation (5) allow us to write the sum of equations (3) and (4) as

$$\frac{D_s \phi}{Dt} = (1 - \phi) \nabla \cdot \mathbf{v}_s - \left[\frac{v_A}{\rho_A} + \frac{v_B}{\rho_B} \right] R, \quad (9)$$

which shows that changes in fluid content (porosity) are a balance of mechanical volumetric strain and reactions. We can use equation (2) to obtain an expression for $\nabla \cdot [\phi \mathbf{v}_f]$:

$$\nabla \cdot [\phi \mathbf{v}_f] = \frac{v_f}{\rho_f} R - \frac{\partial \phi}{\partial t} - \frac{\phi}{\rho_f} \frac{D_f \rho_f}{Dt}, \quad (10)$$

where the last term on the right-hand side represents changes in fluid density. We can then use equation (9) to obtain an expression for $\nabla \cdot [(1 - \phi) \mathbf{v}_s]$:

$$\nabla \cdot [(1 - \phi) \mathbf{v}_s] = \left[\frac{v_A}{\rho_A} + \frac{v_B}{\rho_B} \right] R + \frac{\partial \phi}{\partial t}. \quad (11)$$

Finally, adding equations (10) and (11) yields

$$\nabla \cdot \mathbf{v}_s + \nabla \cdot [\phi (\mathbf{v}_f - \mathbf{v}_s)] = \left[\frac{v_f}{\rho_f} + \frac{v_A}{\rho_A} + \frac{v_B}{\rho_B} \right] R - \frac{\phi}{\rho_f} \frac{D_f \rho_f}{Dt}, \quad (12)$$

which says that volumetric solid strain depends on divergence of the separation flux, changes in liquid density and volume change on reaction, the latter of which can be positive or negative depending on the stoichiometry and relative densities of products and reactants.

2.2. Conservation of Momentum

A quasi-static force balance between the mechanical phases states that

$$\nabla \cdot [\phi \sigma_f] + \phi \rho_f \mathbf{g} + \mathbf{F}_f = \mathbf{0} \quad (13)$$

$$\nabla \cdot [(1 - \phi) \sigma_s] + (1 - \phi) \rho_s \mathbf{g} + \mathbf{F}_s = \mathbf{0}, \quad (14)$$

where σ_f and σ_s are the macroscopic stress tensors for the fluid and solid, and \mathbf{g} is the gravitational acceleration. The interphase forces \mathbf{F}_f and \mathbf{F}_s represent volume-averaged forces at the microscopic fluid-solid interface. Note that positive stresses are tensile.

To close equations (13) and (14) requires constitutive relations for the solid and fluid stresses in terms of pressures, velocities, and/or displacements. As the rheology of the two-phase aggregate should depend only on the stresses associated with its deformation, we formulate the solid stress in terms of an effective stress σ' . This measures the stress in excess of the fluid pressure and is defined in terms of the total stress σ_s and fluid pressure P_f as

$$\sigma' \equiv (1 - \phi) [\sigma_s + P_f \mathbb{I}]. \quad (15)$$

An unconfined, homogeneous region of fluid-infiltrated porous rock that has undergone some amount of reaction will experience a perfectly uniform volume change that is stress-free. This nonelastic strain—or *eigenstrain*—is analogous to, for example, thermal expansion or plastic strain (Mura, 1987; Timoshenko & Goodier, 1970) and has also been considered in the context of reaction-driven fracturing (Ulven et al., 2014). Assuming an isotropic linear elastic solid, the strain e' that is responsible for generating elastic stresses is given by

$$e' = e - e^*, \quad (16)$$

where e is the Cauchy strain tensor and e^* is the eigenstrain due to the reaction. The effective stress σ' can then be written in terms of e' as

$$\sigma' = 2Ge' + \lambda Tr(e'), \quad (17)$$

where G is the elastic shear modulus, λ is the first Lamé parameter, and $K_e = \frac{2G}{3} + \lambda$ is the elastic bulk modulus. Note that the definition of the effective stress in (17) makes the assumption of small strains, though it is possible to extend the theory to finite strain (e.g., MacMinn et al., 2016).

The fluid stress tensor can be expressed in terms of its deviatoric and isotropic components as

$$\sigma_f = \tau_f - P_f \mathbb{I}. \quad (18)$$

At macroscopic scale, the dominant stress in low-viscosity fluid is the pressure as fluctuations in deviatoric stress homogenize to zero (Simpson et al., 2010a, 2010b). This suggests that it is appropriate to assume that the mean deviatoric stress in the fluid is negligible, implying that

$$\sigma_f = -P_f \mathbb{I}. \quad (19)$$

We assume that the fluid and solid experience equal and opposite forces at the interface and that the force exerted on the solid can be written as

$$\mathbf{F}_s = \mathbf{d}(\mathbf{v}_f - \mathbf{v}_s) - P_f \nabla \phi - \nabla e_s, \quad (20)$$

where \mathbf{d} is a (potentially tensor valued) drag coefficient and e_s is the net surface energy of the two-phase aggregate. The first term on the right-hand side of (20) is a frame-independent interaction term that accounts for the relative motion of the fluid and solid at the interface, the second term is the fluid pressure acting normal to the interface, and the final term is the surface tension force. The assumption that $\mathbf{F}_f = -\mathbf{F}_s$ deviates from previous treatments of interfacial tension in the context of two-phase systems (e.g., Drew & Segel, 1971; Bercovici et al., 2001a; Stevenson, 1986), where it is generally assumed that the interphase forces are not equal in the presence of surface tension/energy. While this is the case for two immiscible fluids, it is not clear how this extends to a fluid-infiltrated elastic solid. Moreover, our assumptions lead to a system that is consistent with recent studies of poromechanical swelling (see, e.g., Bertrand et al., 2016), in which the fluid flux is driven by chemical potential gradients.

Substituting (20) and (19) into the fluid momentum equation (13) yields

$$\mathbf{d}(\mathbf{v}_f - \mathbf{v}_s) = -\phi \left[\nabla P_f - \rho_f \mathbf{g} - \frac{1}{\phi} \nabla e_s \right]. \quad (21)$$

As the drag coefficient tensor must be symmetric positive definite—and therefore invertible—we may rewrite the above as

$$\phi(\mathbf{v}_f - \mathbf{v}_s) = -\phi^2 \mathbf{d}^{-1} \left[\nabla P_f - \rho_f \mathbf{g} - \frac{1}{\phi} \nabla e_s \right]. \quad (22)$$

To complete the correspondence with Darcy's law, we set

$$\phi^2 \mathbf{d}^{-1} = \frac{\mathbf{K}_\phi}{\mu}, \quad (23)$$

where μ is the fluid viscosity and \mathbf{K}_ϕ is the permeability tensor. Using (22) and (23) allows us to rewrite (12) as

$$\nabla \cdot \mathbf{v}_s = \nabla \cdot \frac{\mathbf{K}_\phi}{\mu} \left[\nabla P_f - \rho_f \mathbf{g} - \frac{1}{\phi} \nabla e_s \right] + \left[\frac{v_f}{\rho_f} + \frac{v_A}{\rho_A} + \frac{v_B}{\rho_B} \right] R - \frac{\phi}{\rho_f} \frac{D_f \rho_f}{Dt}. \quad (24)$$

Rather than solving (14) directly, we combine (14) and (13) to obtain an equation for the mean stress $\bar{\sigma} \equiv \phi \sigma_f + (1 - \phi) \sigma_s$:

$$\nabla \cdot \bar{\sigma} + \bar{\rho} \mathbf{g} = \mathbf{0}, \quad (25)$$

where $\bar{\rho} = \phi \rho_f + (1 - \phi) \rho_s$. Substituting (15) into (25) yields

$$\nabla \cdot \sigma' - \nabla P_f + \bar{\rho} \mathbf{g} = \mathbf{0}. \quad (26)$$

To summarize, conservation of momentum for the solid is equivalent to equation (26). Conservation of volume/mass coupled to conservation of momentum for the fluid is equivalent to equation (24).

Under the assumption of infinitesimal elastic strains we may assume that $\frac{D}{Dt} \approx \frac{\partial}{\partial t}$, and hence that

$$\nabla \cdot \mathbf{v}_s \approx \frac{\partial}{\partial t} \nabla \cdot \mathbf{u}_s, \quad (27)$$

where \mathbf{u}_s is the total displacement of any particle from its initial configuration. The equation of state for the fluid is expressed as

$$\frac{1}{\rho_f} \frac{\partial \rho_f}{\partial t} = \frac{1}{K_f} \frac{\partial P_f}{\partial t}, \quad (28)$$

where K_f is the bulk modulus of the fluid.

The full system of equations for mass and momentum conservation may now be written as follows:

$$\nabla \cdot \sigma' - \nabla P_f + \bar{\rho} \mathbf{g} = \mathbf{0}, \quad (29)$$

$$\frac{\partial \phi}{\partial t} = (1 - \phi) \nabla \cdot \dot{\mathbf{u}}_s - \left[\frac{v_A}{\rho_A} + \frac{v_B}{\rho_B} \right] R, \quad (30)$$

$$\frac{\partial \phi_A}{\partial t} = -\phi_A \nabla \cdot \dot{\mathbf{u}}_s + \frac{v_A}{\rho_A} R, \quad (31)$$

$$\nabla \cdot \dot{\mathbf{u}}_s + \frac{\phi}{K_f} \frac{\partial P_f}{\partial t} = \nabla \cdot \frac{\mathbf{K}_\phi}{\mu} \left[\nabla P_f - \rho_f \mathbf{g} - \frac{1}{\phi} \nabla e_s \right] + \left[\frac{v_f}{\rho_f} + \frac{v_A}{\rho_A} + \frac{v_B}{\rho_B} \right] R. \quad (32)$$

If we neglect terms due to the reaction and surface tension, then the equations derived above are equivalent to those obtained from the theory of Biot (1941). This equivalence is shown in Appendix A.

3. Constitutive Relations

To solve the system (29)–(32) requires closures for the net surface energy e_s , the permeability \mathbf{K}_ϕ , the eigenstrain ϵ^* , and the reaction rate R . Derivations of their individual forms are described in the subsequent sections. We note that in macroscopic descriptions such as this one, critical constitutive relations depend on the microstructure of pores and grains. There are several techniques that allow closures to be derived in a more rigorous manner (e.g., homogenization or volume averaging); however, for illustrative purposes we consider here a simple consistent formulation based on one particular microstructure. This particular choice yields a tractable and understandable model that clearly highlights the relative contributions of the competing processes in equations (29)–(32), but other choices are possible and can be explored as necessary.

3.1. Surface Energy

We propose that the net surface energy of a cracked or granular medium takes the following form:

$$e_s = \gamma_{ss}\alpha_{ss} + \gamma_{sl}\alpha_{sl}, \quad (33)$$

where for solid-solid contacts we denote γ_{ss} as the surface energy per unit area and α_{ss} as the specific surface area per unit volume. Both γ_{sl} and α_{sl} are defined similarly for solid-liquid contacts. Both α_{ss} and α_{sl} will depend on material properties of the solid, such as total crack density or grain size, and the porosity ϕ . Here we assume that the material properties are fixed, so that the interfacial surface area changes in response to variations in porosity only, although these may evolve once the solid is allowed to deform via recrystallization and/or fracture (e.g., Malvoisin et al., 2017).

Constitutive forms for α_{sl} and α_{ss} will depend on the microstructure of the two-phase medium. Here we consider a microstructure where fluid is distributed within an interconnected network of microcracks. In what follows, we define w as the average wetted crack aperture, N_c as the average number of cracks per unit volume, and A_f and A_s as the average surface area of wetted and unwetted cracks, respectively. If the wetted cracks are assumed to have cross-sectional length l and height h , then the surface area is given by $A_f = 2lh$. We may therefore write α_{sl} as

$$\alpha_{sl} = 2N_c lh, \quad (34)$$

and the porosity ϕ as

$$\phi = N_c lwh, \quad (35)$$

so that

$$\alpha_{sl} = \frac{2\phi}{w}. \quad (36)$$

If we assume that the unwetted cracks have a constant reference length l_0 when $\phi = 0$, then the surface area can be written as $A_s = (l_0 - l)h$, which yields

$$\alpha_{ss} = N_c(l_0 - l)h, \quad (37)$$

which using (34) becomes

$$\alpha_{ss} = N_c l_0 h - \alpha_{sl}/2. \quad (38)$$

Assuming constant N_c and h , we may write the gradient of e_s as

$$\nabla e_s = \left(\gamma_{sl} - \frac{\gamma_{ss}}{2} \right) \nabla \alpha_{sl}. \quad (39)$$

Based on analyses of single isolated veins, Vermilye and Scholz (1995) suggest that crack width and length can be related by

$$w = \delta l, \quad (40)$$

where δ is the crack aspect ratio. This allows to rewrite (35) as

$$\phi = \frac{N_c w^2 h}{\delta}. \quad (41)$$

If we assume that the microstructure is invariant along some axis, then the porosity can be equivalently characterized as an area fraction, meaning that ϕ can absorb a factor of h without changing its interpretation. Under this assumption we can express w in terms of ϕ as

$$w = \left(\frac{\phi \delta}{N_c} \right)^{1/2}. \quad (42)$$

This says that as ϕ is increased, both the width and length will increase while maintaining a constant aspect ratio δ . We may therefore write the gradient of e_s as

$$\nabla e_s = -\Delta\gamma \left(\frac{N_c}{4\delta\phi} \right)^{1/2} \nabla \phi, \quad (43)$$

where $\Delta\gamma = \frac{\gamma_{ss}}{2} - \gamma_{sl}$. The surface energy term in (43) drives fluid flow in the direction of decreasing or increasing porosity, depending on the sign of $\Delta\gamma$.

3.2. Permeability

Under the assumption that the porous medium is isotropic, we may replace the permeability tensor \mathbf{K}_ϕ by a scalar K_ϕ . Following Gueguen and Dienes (1989), we use the following form for K_ϕ :

$$K_\phi = Cw^2\phi, \quad (44)$$

where w is the crack width and C is a constant that depends on the pore geometry ($C \approx 1/3$ in this case). Substituting equation (42) into the above yields

$$K_\phi = w_0^2\phi^2, \quad (45)$$

where w_0 is a reference crack width, which is defined as

$$w_0 = \left(\frac{C[\phi]\delta}{N_c} \right)^{1/2}, \quad (46)$$

where $[\phi]$ is the reference value used in the porosity scaling.

3.3. Eigenstrain

To determine an appropriate form for the eigenstrain due to the reaction ϵ^* , we first consider the evolution of a general spatial coordinate $\mathbf{x}(t)$ for a piece of material. A basic decomposition of $\mathbf{x}(t)$ is

$$\mathbf{x}(t) = \mathbf{x}_0(t) + \mathbf{u}'_s(t), \quad (47)$$

where $\mathbf{x}_0(t)$ is the coordinate of the *equilibrium* reference system that is stress-free, and $\mathbf{u}'_s(t)$ are displacements from equilibrium that lead to elastic stresses. It follows that the solid velocity $\mathbf{v}_s = \dot{\mathbf{x}}(t)$, which can be substituted into the left-hand side of (24). Assuming that $\mathbf{x}_0(t)$ is controlled by the reaction and that the elastic stresses only depend on $\mathbf{u}'_s(t)$, it follows that the eigenstrain can be written as

$$\epsilon^* = (\nabla \cdot \dot{\mathbf{x}}_0)\mathbb{I}, \quad (48)$$

which using (24) implies that

$$\epsilon^* = \left(\int_0^t \nabla \cdot \dot{\mathbf{x}}_0(t') dt' \right) \mathbb{I} \quad (49)$$

$$= \left(\int_0^t R^*(t') dt' \right) \mathbb{I}, \quad (50)$$

where $R^*(t) = \left[\frac{v_f}{\rho_f} + \frac{v_A}{\rho_A} + \frac{v_B}{\rho_B} \right] R$. Again, we note that R^* can be positive or negative (where $R > 0$ for a forward reaction) depending on the relative stoichiometry and density of reactants and products.

3.4. Reaction Rate

For systems that are out of equilibrium, the theory of nonequilibrium thermodynamics (De Groot & Mazur, 1962; Prigogine, 1967) states that chemical processes are driven by the degree of disequilibrium or the affinity. The affinity A is a scalar measure of disequilibrium for the system, which for a general reaction is defined as

$$A = -\Delta_r G = - \sum_{i,k} v_i^k \mu_i^k, \quad (51)$$

where $\Delta_r G$ is the Gibbs free energy of the reaction and μ_i^k and v_i^k are the chemical potential and stoichiometric coefficient of component k in phase i , respectively. The above is summed over all phases and components. We note that, in equilibrium, the chemical potential of every component in every phase is equal, that is, $\mu_i^k = \mu_j^k$ for component k in phases i and j . As conservation of mass requires that $\sum_{i,k} v_i^k = 0$, this implies that $A = 0$ when the system is in equilibrium. Peridotite and water can only be in equilibrium at high temperatures (see, e.g., phase diagram 4 (d) in van Keken et al., 2011). As we are considering processes at near-surface conditions (low P and T), it is unlikely that any changes in temperature are large enough to moderate the reaction: any fluid that is present will likely be exhausted before the system reaches equilibrium. It would therefore seem reasonable to assume that $\Delta_r G$ is constant in what follows; however, in higher temperature settings (e.g., a subducting slab) this will not be the case.

We propose that the reaction rate R is proportional to the chemical affinity A , a kinetic rate constant r , and the available reactive surface area a . Although beyond the scope of this paper, the kinetic rate r will be affected by changes in temperature and pressure. For the available surface area we will assume a to take the form suggested by Rudge et al. (2010):

$$a = a_0 \phi \phi_A, \quad (52)$$

where a_0 is a reference reactive surface area (per unit volume), which we assume to be equal to the inverse of the reference crack width $1/w_0$. Although we have chosen a particular form for the available surface area function a , we could have equally chosen any suitable function subject to the constraint that $a \rightarrow 0$ as $\phi \rightarrow 0$ and $\phi_A \rightarrow 0$. In practice, a should represent (macroscopically) the effect of the changing microstructure with reaction progress. In particular, it should describe the effect of armoring of reactive surfaces. Although the choice of a in (52) does not explicitly capture the effect of armoring, it could do by, for example, adding the modification that $a = 0$ for $\phi_B > \phi_B^{\text{crit}}$, which is to say that there is some critical amount of solid product ϕ_B^{crit} that *armors* the wall of the pore space to prohibit any further reaction.

The simplest form for the reaction rate R given the above assumptions is as follows:

$$R = m_B r a_0 \frac{A}{R_s T} \phi \phi_A, \quad (53)$$

where R_s is the universal gas constant ($\text{J} \cdot \text{mol}^{-1} \cdot \text{K}^{-1}$), T is temperature (K), and m_B is the molecular weight of serpentine (kg/mol). The factor of $1/R_s T$ has been included in order to make the thermodynamic disequilibrium term nondimensional.

4. Scaling

To nondimensionlize equations (29)–(32) we introduce the following scalings:

$$\begin{aligned} \mathbf{x} &= [x] \mathbf{x}', & (\phi, \phi_A) &= ([\phi] \phi', [\phi_A] \phi'_A), \\ (K_e, G) &= [K_e] (K'_e, G'), & t &= \frac{[x]}{[v_f]} t', \\ K_\phi &= [K_\phi] K'_\phi, & P_f &= [P_f] P'_f, \\ \mathbf{u}_s &= [u_s] \mathbf{u}'_s \end{aligned}$$

where primed terms represent dimensionless variables and bracketed terms represent their characteristic scalings. The characteristic separation flux $[v_f]$ is given by

$$[v_f] = \frac{[K_\phi][P_f]}{\mu[x][\phi]}, \quad (54)$$

where the reference permeability is $[K_\phi] = w_0^2[\phi]$ and the reference crack width w_0 is defined in equation (45). From equation (29) we observe that a natural choice for the reference fluid pressure is $[P_f] = [\phi][K_e]$, which is the pressure change in response to a volumetric strain of $[\phi]$ for a solid with an elastic bulk modulus of $[K_e]$. Substituting this choice for $[P_f]$ into equation (29) yields a reference solid displacement of $[u_s] = [x][\phi]$.

These scalings allow us to rewrite the system of equations (29)–(32) in terms of dimensionless variables as (dropping primes)

$$\nabla \cdot \boldsymbol{\sigma}'_s - \nabla P_f + \frac{\mathcal{G} \bar{\rho}}{\rho_f} \hat{\mathbf{g}} = \mathbf{0}, \quad (55)$$

$$\frac{\partial \phi}{\partial t} = (1 - [\phi]) \nabla \cdot \dot{\mathbf{u}}_s + R_\phi \phi \phi_A, \quad (56)$$

$$\frac{\partial \phi_A}{\partial t} = -[\phi] \phi_A \nabla \cdot \dot{\mathbf{u}}_s + R_{\phi_A} \phi \phi_A, \quad (57)$$

$$\nabla \cdot \dot{\mathbf{u}}_s + \beta \phi \frac{\partial P_f}{\partial t} = \nabla \cdot K_\phi \left[\nabla P_f - \mathcal{G} \hat{\mathbf{g}} + \frac{\mathcal{E}}{\phi^{1/2}} \nabla \phi \right] + R_{P_f} \phi \phi_A, \quad (58)$$

where the elastogravity number \mathcal{G} , elastocapillary number \mathcal{E} , Damköhler number Da , and relative fluid compressibility β are the dimensionless parameters given by

$$\mathcal{E} = \frac{\Delta \gamma}{w_0 [\phi] [K_e]}, \quad (59)$$

$$\mathcal{G} = \frac{\rho_f g [x]}{[\phi][K_e]}, \quad (60)$$

$$Da = \frac{R' [x] v_A [\phi_A]}{[v_f] \rho_A}, \quad (61)$$

$$\beta = \frac{[\phi][K_e]}{K_f}, \quad (62)$$

where $R' = m_B r a_0 A / R_s T$ and $\Delta\gamma$ has been redefined to absorb a factor of $\frac{c^{1/2}}{2}$. Parameters R_ϕ , R_{ϕ_A} , and R_{ρ_f} are scaled Damköhler numbers that are defined as follows:

$$R_\phi = Da \left[1 + \frac{v_B \rho_A}{v_A \rho_B} \right], \quad (63)$$

$$R_{\phi_A} = -Da \frac{[\phi]}{[\phi_A]}, \quad (64)$$

$$R_{\rho_f} = -Da \left[1 + \frac{v_f \rho_A}{v_A \rho_f} + \frac{v_B \rho_A}{v_A \rho_B} \right]. \quad (65)$$

4.1. Interpretation of Dimensionless Parameters

The elastocapillary number \mathcal{E} represents the ratio of surface tension to elastic forces. We would expect surface tension to play a significant role in solid deformation at lengthscales smaller than the elastocapillary lengthscale $\delta_\mathcal{E} \equiv \Delta\gamma / [\phi][K_e]$, that is, when

$$w_0 < \delta_\mathcal{E}. \quad (66)$$

Similarly, gravitational effects will be important when the system size $[x]$ is larger than the elastogravity lengthscale $\delta_\mathcal{G} \equiv [K_e][\phi] / \rho_f g$, which is the scale over which buoyancy forces are large enough to cause volume changes of order $[\phi]$. The elastogravity number \mathcal{G} describes the ratio of these lengthscales.

We may also consider the ratio of buoyancy forces to surface tension, which is represented by the Bond number Bo :

$$Bo \equiv \frac{\mathcal{G}}{\mathcal{E}} = \frac{\rho_f g [x] w_0}{\Delta\gamma}. \quad (67)$$

This is independent of elastic forces and is small when surface tension is stronger than buoyancy.

The Damköhler number Da is the ratio of the reactive and fluid transport timescales. When the Damköhler number is large we would observe more reaction progress during the time taken to transport the fluid by a distance $[x]$, and less reaction progress when it is small.

5. Model Setup

The hydration of peridotite exposed at the seafloor is a key process in the subduction zone water cycle, having critical implications for arc magmatism and volatile cycling. Alteration of the oceanic plate is especially apparent in tectonic settings where significant fracturing/faulting allows seawater to percolate into the lithosphere, for example, near slow-ultra slow spreading ridges, fracture zones, and trench-outer rise regions (Faccenda, 2014). Such environments therefore serve as a pertinent setting to apply this model. In particular, we considered a region of peridotite at the seafloor, which includes a fluid-rich vertical fracture connected to the overlying seawater. The specific details of the model setup are described in the remainder of this section.

The model domain is a rectangle that is 120-m wide and 100-m high, where the top boundary ($z = 0$) represents the seafloor. We take the seafloor depth to be 1,000 m, which is comparable to the depth of the Lost City hydrothermal field (Kelley et al., 2005). The fluid-rich fracture/fault zone is approximately 1-m wide, beginning at the center of the top boundary and extending vertically down to a depth of 50 m. The material in the fracture zone is still considered mechanically intact but has an elevated porosity relative to the background. We set the initial background porosity to be 0.1% and represent the initial fracture zone porosity by ϕ_0^c , which is assumed to be in the range of 1–10%. Although the permeability in the fracture zone depends on the porosity (see equation (45)), we also allow it to vary by a constant, dimensionless scaling factor K_ϕ^c to account for changes in tortuosity.

We assume that the fluid pressure is continuous at the top boundary and initially hydrostatic with depth. A seafloor depth of 1,000 m implies that the fluid pressure is $P_f^{\text{seafloor}} \approx 10$ MPa at the top boundary. The fluid flux and displacement normal to the boundary at the sides and bottom are zero. Both the tangential and normal components of the effective stress normal to the top boundary are zero, that is, $\sigma' \cdot \mathbf{n}|_{z=0} = \mathbf{0}$. We assume that the system is initially in hydrostatic equilibrium, so that the initial condition for the displacement is the solution to equation (55) given the stated stress/displacement boundary conditions and the hydrostatic initial condition for the fluid pressure $P_f|_{t=0} = P_f^{\text{seafloor}} - \mathcal{G}z$. We also assume that the system is initially unserpentinized ($\phi_B|_{t=0}$), which implies that $\phi_A|_{t=0} = 1 - \phi|_{t=0}$.

5.1. Parameters

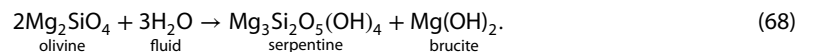
5.1.1. Physical Parameters

Equation (46) relates the reference crack width w_0 to the reference porosity $[\phi]$, the crack density N_c , and the crack aspect ratio δ . For crack densities in the range of $10^8 - 10^{12}$ (Hadley, 1976), an aspect ratio of $\delta = 10^{-3}$ (Vermilye & Scholz, 1995) and a reference porosity of $[\phi] = 10\%$, we estimate the reference crack width to lie in the range of $w_0 \sim 10^{-8} - 10^{-6}$ m. This range of crack widths implies reference permeabilities ranging between $[K_\phi] \sim 10^{-17} - 10^{-13}$ m², which would lead to a permeability range of $K_\phi \sim 10^{-15} - 10^{-11}$ m² in the fracture zone if 1% porosity is assumed. Estimates of permeabilities for upper crust mantle periodotites are dependent on scale and depth: observations suggest $10^{-13} - 10^{-10}$ m² for shallow depths over large scales (Wu et al., 2006) and $10^{-17} - 10^{-14}$ m² for greater depths over small scales (Manning & Ingebritsen, 1999). Hydrogeologic studies in the Oman ophiolite also estimate that a fissured near-surface horizon has a permeability of 10^{-14} m² (Dewandel et al., 2005). These suggest that our estimated permeabilities are reasonable, and where the permeabilities in the fracture zone are particularly high, we may adjust K_ϕ by increasing the scaling factor K_ϕ^c .

From Abramson et al. (1997), the value of the bulk and shear moduli of San Carlos olivine at zero-confining pressure are $K_e = 129.4$ GPa and $G = 78.0$ GPa. We note these values are likely to be an overestimate for this problem as the elastic moduli will ultimately depend on the porosity and crack density; however, for simplicity we assume that K_e and G are constant, with a reference bulk modulus of $[K_e] = 10^{11}$ Pa. Using a fluid bulk modulus of $K_f = 2.2 \times 10^9$ Pa with this reference bulk modulus yields a dimensionless fluid compressibility of $\beta \approx 4.55$ (for $[\phi] = 0.1$); as our simulations show that this value of β has negligible effect on the overall behavior, we assume its value to be zero for the remainder of this paper. Experimentally derived surface energies suggest that $\gamma_{ss} \sim 0.25 - 4$ J/m² (Atkinson & Avdis, 1980; Kelemen & Hirth, 2012; Tapponnier & Brace, 1976). Studies on quartz-water (Parks, 1984) and melt-olivine (Riley & Kohlstedt, 1991) systems suggest solid-liquid interfacial energies of ~ 0.3 J/m² and ~ 0.5 J/m², respectively. As these values are similar (for very different systems), it seems reasonable to assume that $\gamma_{sl} \sim 0.3 - 0.5$ J/m².

5.1.2. Reaction Rate

This reaction involves the conversion of water and olivine into the hydrous phases serpentine and brucite:



The corresponding densities and molar masses for this reaction are summarized in Table 1. At constant temperature and confining pressure, the change in the Gibbs free energy for this reaction is given by

$$\Delta_r G = -R_s T \ln(\Omega), \quad (69)$$

where Ω is the ratio of the product of stoichiometric activities and the equilibrium reaction coefficient. For near-surface serpentinization of olivine it is observed that $\Omega \sim 10^7$ (Kelemen & Hirth, 2012), which is large due to the fact that olivine is very far out of equilibrium with water under these conditions. Using the fact that the affinity $A = -\Delta_r G$, we may write

$$\frac{A}{R_s T} = \ln \Omega \sim \ln(10^7). \quad (70)$$

Experimentally derived rates of serpentinization in the literature are highly variable (Lafay et al., 2012; Lamadrid et al., 2017; Malvoisin et al., 2012; Martin & Fyfe, 1970; McCollom et al., 2016; Ogasawara et al., 2013; Wegner & Ernst, 1983) and temperature dependent. Rates in the aforementioned studies range from 10^{-10} to 10^{-7} mol·m⁻²·s⁻¹ for temperatures in the range of 200–400 °C. The temperature will vary considerably depending on the proximity to the ridge axis, for example, at Lost City where seafloor temperatures can

Table 1
Table of Parameters

Definition (unit)	Symbol	Value
System size (m)	$[x]$	100
Reference porosity	$[\phi]$	0.1
Reference phase A (olivine) fraction	$[\phi_A]$	1
Characteristic microcrack width (m)	w_0	$10^{-8} - 10^{-6}$
Crack aspect ratio	δ	10^{-3}
Crack density (m^{-3})	N_c	$10^8 - 10^{12}$
Reference permeability (m^2)	$[K_\phi]$	$10^{-17} - 10^{-13}$
Initial fracture porosity (%)	ϕ_0^c	1–10
Surface energy of solid-solid contacts (J/m^2)	γ_{ss}	0.25–4
Surface energy of solid-liquid contacts (J/m^2)	γ_{sl}	0.3–0.5
Reaction coefficient	Ω	1×10^7
Kinetic rate constant ($\text{mol}\cdot\text{m}^{-2}\cdot\text{s}^{-1}$)	r	$10^{-12} - 10^{-8}$
Viscosity of water ($\text{kg}\cdot\text{s}^{-1}\cdot\text{m}^{-1}$)	μ	8.90×10^{-4}
Reference bulk modulus (Pa)	$[K_e]$	10^{11}
Dimensionless bulk modulus	K_e	1
Dimensionless shear modulus	G	0.5
Damköhler number	Da	$10^{-6} - 10^2$
Elastocapillary number	\mathcal{E}	$10^{-4} - 10^{-2}$
Elastogravity number	\mathcal{G}	9.81×10^{-5}
Density of olivine (kg/m^3)	ρ_A	3,300
Density of serpentine (kg/m^3)	ρ_B	2,537
Density of water (kg/m^3)	ρ_f	1,000
Molecular weight of olivine (kg/mol)	m_A	0.281
Molecular weight of serpentine (kg/mol)	m_B	0.335
Molecular weight of water (kg/mol)	m_f	0.055

reach up to 150 °C (Seyfried et al., 2015). Fitted serpentinization rates as function of temperature suggest that these rates may decrease by ~ 1 –4 orders of magnitude for temperatures in the range of 50–150 °C (Kelemen & Matter, 2008). Moreover, recent experiments by Lamadrid et al. (2017) show that the rate of serpentinization is heavily influenced by fluid salinity. Given the large uncertainty it seems reasonable that r will vary by several orders of magnitude. For $T \sim 100$ –150 °C we could therefore consider rates in the range of $r \sim 10^{-12} - 10^{-8} \text{ mol}\cdot\text{m}^{-2}\cdot\text{s}^{-1}$.

6. Results

Equations (55)–(58) with the initial and boundary conditions described above, together with parameters appropriate for seafloor serpentinization were solved using the open-source software TerraFERMA (Wilson et al., 2017) which provides a flexible framework for constructing reproducible Finite Element Models from advanced computational libraries (FEniCS; Alnaes et al., 2015, and PETSc; Balay et al., 2001). Appendix B provides details of the numerical methods. The TerraFERMA input files (which contain all information, including equations) for reproducing the models shown in this paper are available in the git repository, https://github.com/orevans/poroelastic_serpentinization.

6.1. Basic Behavior

Figure 1 shows a typical set of results in the absence of surface energy ($\mathcal{E} = 0$). This particular simulation used a crack permeability factor of $K_\phi^c = 100$ and a Damköhler number of $Da \approx 22.7$. This value of Da was calculated with an effective reaction rate of $R' = 10^{-3} \text{ kg}\cdot\text{m}^{-3}\cdot\text{s}^{-1}$, which assumes a kinetic rate constant of $r \approx 10^{-11} \text{ mol}\cdot\text{m}^{-2}\cdot\text{s}^{-1}$ and a reference crack width of $w_0 = 10^{-8} \text{ m}$. The initial porosity in the fracture zone is $\phi_0^c = 2\%$. All other parameters are set to their respective values in Table 1. This particular simulation was run to a nondimensional time of $t = 4$ (equivalent to ~ 1 year). The results in Figure 1 show a snapshot of the

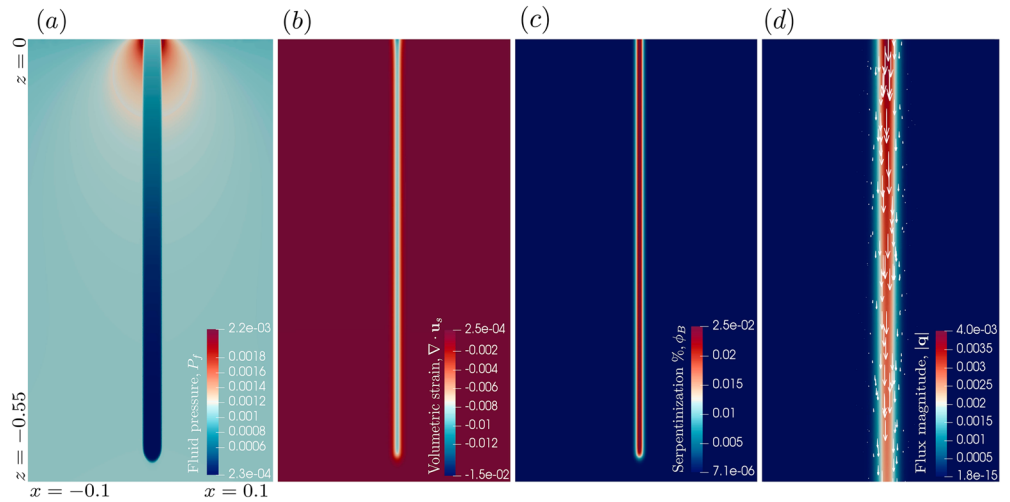


Figure 1. Results at dimensionless time $t = 0.5$ (~ 0.125 years in this model) for (a) fluid pressure P_f , (b) total solid volumetric strain $\nabla \cdot \mathbf{u}_s$, (c) degree of serpentinization ϕ_B , and (d) magnitude of the fluid flux $|\mathbf{q}| = |K_\phi(\nabla P_f - \mathcal{G})|$. Parameters used were $K_\phi^c = 100$, $Da = 22.7$, $r \approx 10^{-11}$ mol·m $^{-2}$ ·s $^{-1}$, $w_0 = 10^{-8}$ m, and $\phi_0^c = 2\%$. There is no surface energy ($\mathcal{E} = 0$) and all other parameter values are given in Table 1. The minimum pressure is 2.3 MPa, the minimum volumetric strain is -0.15% , and the maximum degree of serpentinization is 2.5%. The arrows indicate the direction of fluid flow, and their lengths are scaled to the magnitude $|\mathbf{q}|$.

solution at $t = 0.5$, at which time the fluid fraction is approximately half its initial value ($\phi \sim 1\%$ in the fracture zone). Figure 1c shows that by $t = 0.5$ the degree of serpentinization ϕ_B has reached $\sim 2.5\%$ in the fracture zone. Figure 2b shows the time evolution of ϕ and ϕ_B at a point in the center of the fracture zone, which shows that by $t = 4$ the fluid has been almost entirely exhausted $\phi \approx 0$, leading to $\sim 5.2\%$ serpentinization. The exponentially decaying rate of fluid consumption/serpentine production is due to the $\phi\phi_A$ dependency in the reaction rate.

Figure 1b shows negative volumetric strains in the fracture zone at $t = 0.5$. This result is a simple consequence of the relative densities of water, olivine and serpentine. In particular, the calculated net volume change on reaction (per unit mass), ΔV , for the serpentinization reaction is

$$\Delta V \equiv \left[\frac{V_A}{\rho_A} + \frac{V_f}{\rho_f} + \frac{V_B}{\rho_B} \right] \approx -2.42 \times 10^{-5} \text{ m}^3/\text{kg}, \quad (71)$$

which is negative because this reaction is essentially replacing a low-density fluid with a solid that is closer in density to olivine than it is to water. A closed system of olivine and water would necessarily reduce in volume.

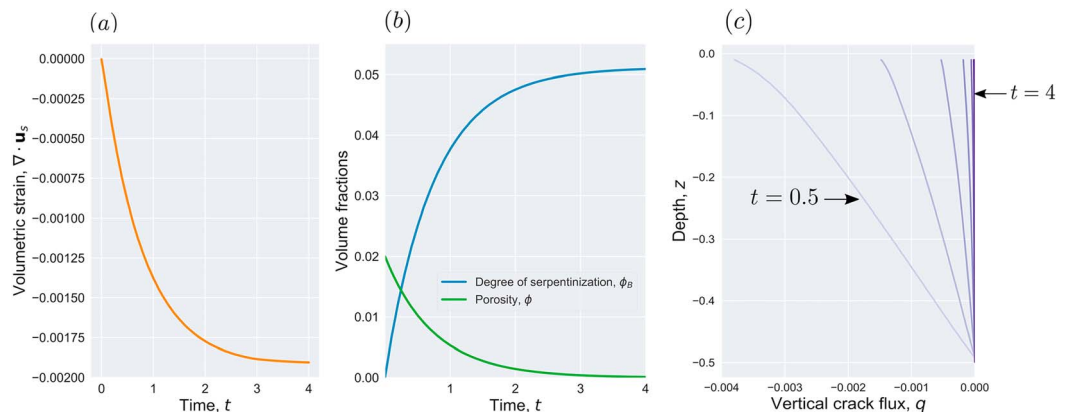


Figure 2. Full time evolution between $t = 0$ and $t = 4$ for (a) volumetric strain $\nabla \cdot \mathbf{u}_s$ and (b) both porosity ϕ and degree of serpentinization ϕ_B ; (c) the vertical component of the flux q at the center of the fracture zone ($x = 0$) as a function of depth z . We note that negative flux implies downward flow. The curves in panel (c) show the solution at uniformly spaced times between $t = 0.5$ and $t = 4$.

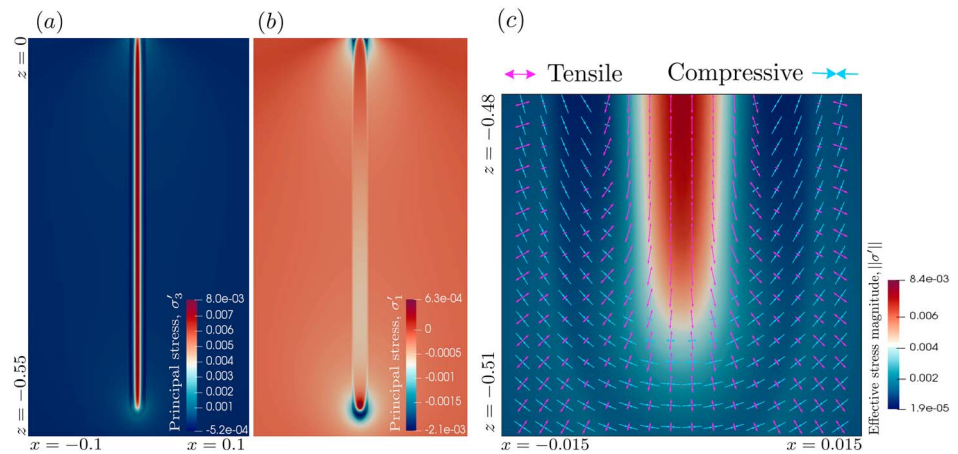


Figure 3. Results at $t = 0.5$ for (a) the most tensile principal stress σ'_3 , (b) the most compressive principal stress σ'_1 and (c) the directions and orientations of the principal axes close to the tip of the fracture zone. The maximum tensile stress (shown in a) is 80 MPa and the minimum compressive stress (shown in b) is -21 MPa. The orientations of the tensile and compressive stresses in (c) are represented by the pink and blue arrows, respectively, and the principal axes have been scaled so that the direction corresponding to the largest principal stress (in absolute value) is unit length. The background colors show the magnitude of the effective stress, where red is high and blue is low.

The volumetric strain in the background is positive as it must expand to accommodate the contraction of the reacting material. Figure 1a shows that the removal of fluid by the reaction leads to subhydrostatic pressures in the fracture zone (~ 2 MPa). The evolution of the volumetric strain at a point in the center of the fracture zone is shown in Figure 2a, which indicates that the net volume change due to the reaction is negative and monotonic decreasing with time. Figure 1d shows the magnitude and direction of the fluid flux close to the upper boundary: negative pressure gradients along the fracture causes downward pumping of fluid, as indicated by the direction of the arrows. Figure 2c shows the vertical component of the flux q in the fracture zone as a function of depth and time, where the different curves show q at uniformly spaced times between $t = 0.5$ and $t = 4$. The magnitude of the flux increases toward the seafloor as the pressure gradient steepens, and the overall flux decreases with time because, as porosity is consumed by the reaction, the permeability will decrease due to its dependence on ϕ^2 .

Figures 3a and 3b show the principal stresses of the effective stress tensor σ' , corresponding to the directions of most compressive (σ'_1) and most tensile (σ'_3) stress, respectively. These have been evaluated at $t = 0.5$. The principal axes in the vicinity of the fracture zone tip are shown in Figure 3c: the background color indicates the magnitude of the effective stress tensor $||\sigma'||$ (high is red, low is blue), and each orthogonal pair has been scaled such that the direction corresponding to the largest principal stress (in magnitude) has been normalized. Panels (a) and (b) show that the dominant principal stress in the fracture zone is tensile (~ 80 MPa), and panel (c) indicates that these stresses are oriented vertically. The contraction of the system in this region causes the material outside it to stretch, resulting in tensile stresses. Here orientations of the most tensile stresses (pink arrows) are roughly orthogonal to the edge of the fracture zone.

Figure 4 shows the locations and orientations of the mode I cracks that would form for a given uniaxial tensile strength T_u . As these are evaluated at the final run time ($t = 4$), it is understood that some regions will have already failed prior to this. The values for T_u in panels (a)–(d) are motivated by experiments suggesting the tensile strength of peridotite to be in the range of 5–20 MPa (Cai, 2010). For ratios of uniaxial tensile to compressive strengths between 1/8 and 1/20 (Paterson, 1978; Scholz, 2002) the model predicts that tensile failure will precede shear failure for any given T_u in this range; therefore, we only consider the mode I failure that would occur from the stress field that we calculate. For all values of T_u in this range the fracture zone is lined with horizontally oriented cracks at all depths. As T_u is decreased cracks begin to form around the tip and top of the fracture zone, oriented parallel to its edge. As T_u is decreased further the damaged area around these regions increases and the parallel-oriented cracks form progressively further away from the top/tip.

6.2. Varying the Fluid Supply

The stresses and amount of reaction that are possible depend on the availability of fluid. In this model we can control this by varying the initial porosity and permeability in the fracture zone. The effects of the permeability

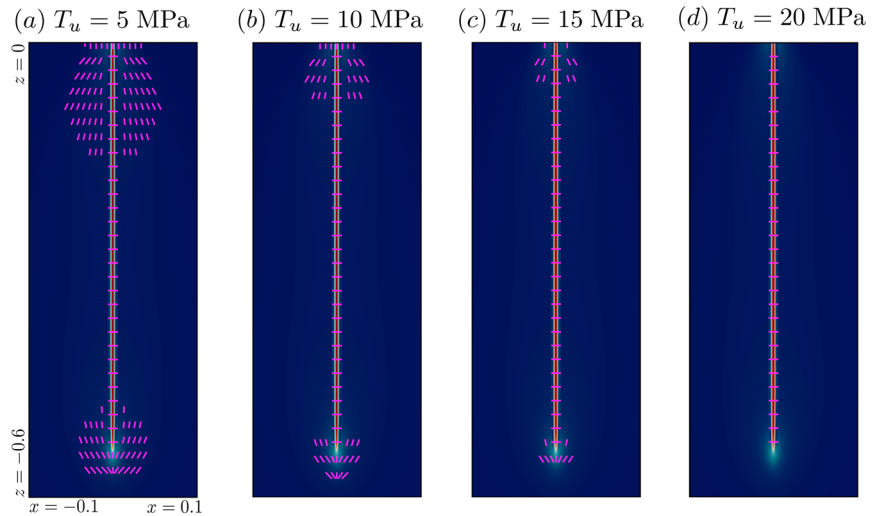


Figure 4. The pink dashes represent the locations and orientations of the mode I cracks that would open up given a uniaxial tensile strength T_u of (a) 5 MPa, (b) 10 MPa, (c) 15 MPa, and (d) 20 MPa. These are evaluated from the stress field at $t = 4$. The background color indicates the magnitude of the effective stress (red is high, blue is low).

and initial porosity on the stress and degree of serpentinization are shown in the top and bottom rows of Figure 5, respectively. Although the permeability is varied by changing the scaling factor K_ϕ^c , we find that the solutions collapse for constant K_ϕ^c/Da , which is because K_ϕ^c/Da is essentially a proxy for the net fluid supply in the time that the reaction substantially reduces the permeability. We therefore treat K_ϕ^c/Da as the independent variable. In these simulations we used logarithmically spaced values of K_ϕ^c/Da between 10^{-5} and 10^3 .

Figures 5a and 5b show the degree of serpentinization ϕ_B and most tensile principal stress σ'_3 evaluated at $t = 0.5$, respectively, as a function of K_ϕ^c/Da , where each point represents the average of that field along the centered vertical axis of the fracture zone ($x = 0, -0.5 \leq z \leq 0$). The upper limit (dotted line) in panel (a) is when all of the physical volume change is accommodated by reaction, that is, $\nabla \cdot \mathbf{u}_s = \nabla \cdot \mathbf{x}_0$, which implies that $\nabla \cdot \mathbf{u}'_s = 0$ (see equation (47)). This occurs when the fluid replacement by pressure-driven downward pumping of fluid is maximized, resulting in more serpentinization because the time-integrated fluid supply, and hence the net fluid available for the reaction, is greater. The lower bound represents the solution in the limit that the permeability goes to zero; there is no fluid replacement in this case. The degree of serpentinization in the fracture zone is approaching the upper bound when $K_\phi^c/Da \gtrsim 100$ and the lower bound when $K_\phi^c/Da \lesssim 10^{-4}$.

Panel (b) shows the average of the most tensile principal stress σ'_3 (in the fracture zone) as a function of K_ϕ^c/Da . When the rate of fluid supply is fast the reaction-driven net strain is more significant, leading to larger tensile stresses. On the other hand, when the permeability is small the overall fluid supply—and therefore the total amount of reaction—is reduced; hence, the tensile stresses are smaller. Panel (c) shows that the average degree of serpentinization in the fracture zone scales linearly with the initial fracture porosity ϕ_0^c for fixed K_ϕ^c/Da (0.05 in this case). Panel (d) shows that the maximum value of σ'_3 (most tensile stress) also scales linearly with ϕ_0^c for this value of K_ϕ^c/Da . The most tensile stress ($\sigma'_3 \sim 350$ MPa) occurs when the starting porosity is maximized ($\phi_0^c = 10\%$). One would expect that the maximum amount of serpentinization (and therefore reactive stress) should be linearly proportional to the initial porosity as that controls the amount of reaction in a closed system. Calculations that vary the initial porosity (Figures 5c and 5d) show this linear increase.

6.3. Surface Energy

In the calculations so far, we have neglected surface energy, which may provide an additional diffusive mechanism for fluid migration from regions of high to low porosity. The significance of this kind of behavior is determined by the dimensionless parameter \mathcal{E} , which depends on the characteristic crack width w_0 and the relative surface energies between fluid and solid $\Delta\gamma = \frac{\gamma_{ss}}{2} - \gamma_{sl}$. For the ranges of surface energies discussed in section 5.1 we expect the fluid to be wetting, that is, that $\mathcal{E} > 0$. A typical set of results for simulations that include surface energy are shown in Figure 6; this run used an initial fracture porosity of $\phi_0^c = 2\%$, a characteristic crack width of $w_0 = 10^{-7}$ m and a surface energy difference of $\Delta\gamma = 1$, which is consistent with the

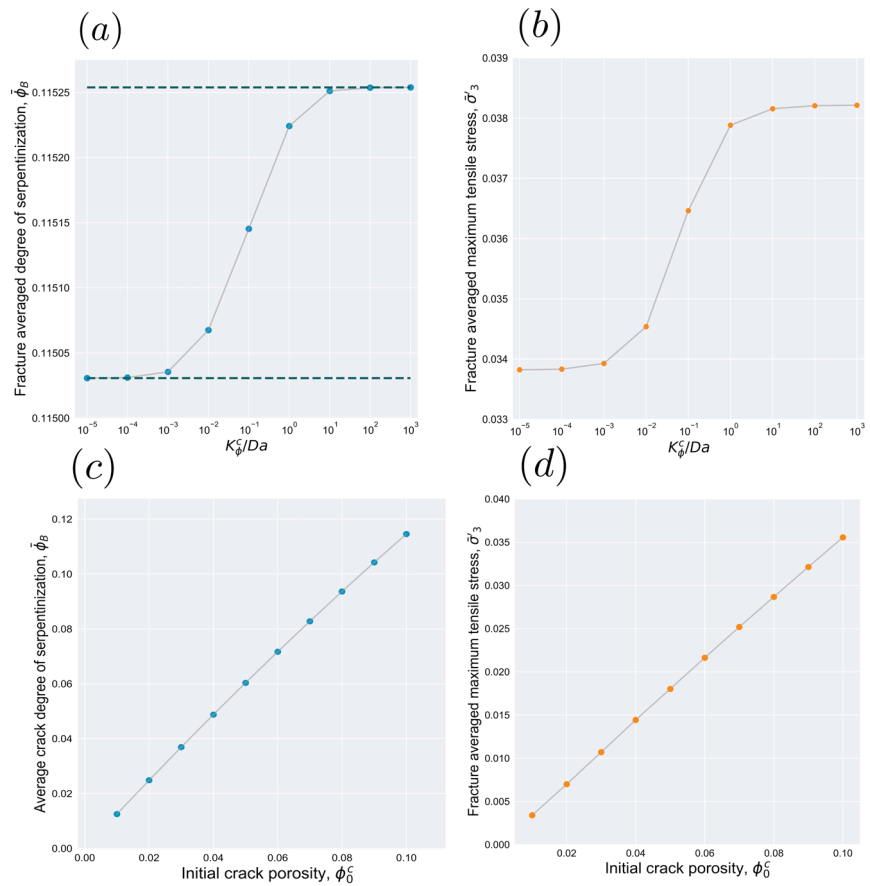


Figure 5. (top row) Results at $t = 0.5$ for the fracture averaged (a) degree of serpentinization $\bar{\phi}_B$ and (b) most tensile principal stress $\bar{\sigma}'_3$ as a function of the crack permeability factor to Damköhler number ratio K_ϕ^c/Da . The plotted points show the average of each field down the center of the fracture zone ($x = 0, -0.5 \leq z \leq 0$). Each simulation used an initial fracture porosity of $\phi_0^c = 10\%$, a reference crack width of $w_0 = 10^{-8}$ m and included no surface energy. The dotted lines in (a) represent the upper and lower bounds on the degree of serpentinization. (bottom row) Results at the same t for the (a) fracture averaged degree of serpentinization $\bar{\phi}_B$ and (b) maximum tensile principal stress as a function of the initial fracture porosity ϕ_0^c (varied between 1% and 10%). These simulations used a crack permeability to Damköhler number ratio of $K_\phi^c/Da = 0.05$, a reference crack width of $w_0 = 10^{-8}$ m and included no surface energy.

range of values discussed in section 5.1. This yields an elastocapillary number of $\mathcal{E} = 10^{-3}$ and a Damköhler number of $Da \approx 0.227$. All other parameters are identical to those used in section 6.1.

Figure 6 shows results for the fluid pressure, volumetric strain, and principal stresses at $t = 0.5$. These simulations have been run for a shorter time so as to limit the amount of reaction that has taken place, which is designed to isolate the behavior of the mechanical swelling. We note, however, that the fast initial transient behavior due to surface energy will be followed by the slower effect of the reaction terms, which will ultimately change the stresses and potentially the orientation of failure. The results shown in Figure 6 demonstrate the fundamental behavior introduced by the surface energy term in equation (58). The fluid fraction decreases rapidly with distance from the fracture zone, resulting in a large, negative porosity gradient. The sign of the surface energy term is therefore negative ($\mathcal{E} \nabla \phi < 0$), leading to fluid migration outward from the fracture zone. As fluid infiltrates the low-porosity zone around its edge, the solid framework swells and the fluid pressure increases. The positive pressures ($P_f \approx 32$ MPa) and volumetric strains ($\nabla \cdot \mathbf{u}_s \approx 0.015\%$) in this region are shown in Figures 6a and 6b, respectively. The principal stresses in panels (c) and (d) tell a similar story: swelling around the edge of the fracture zone (due to fluid infiltration) results in tensile stresses, with a maximum tensile stress of $\sigma'_3 \approx 22$ MPa—this exceeds the tensile strength of peridotite.

Figure 7a shows the principal axes near the fracture zone tip. Inside the overpressured rim (shown in red) the stresses are tensile along both principal axes. The orientations of the σ'_3 axis imply that tensile failure will

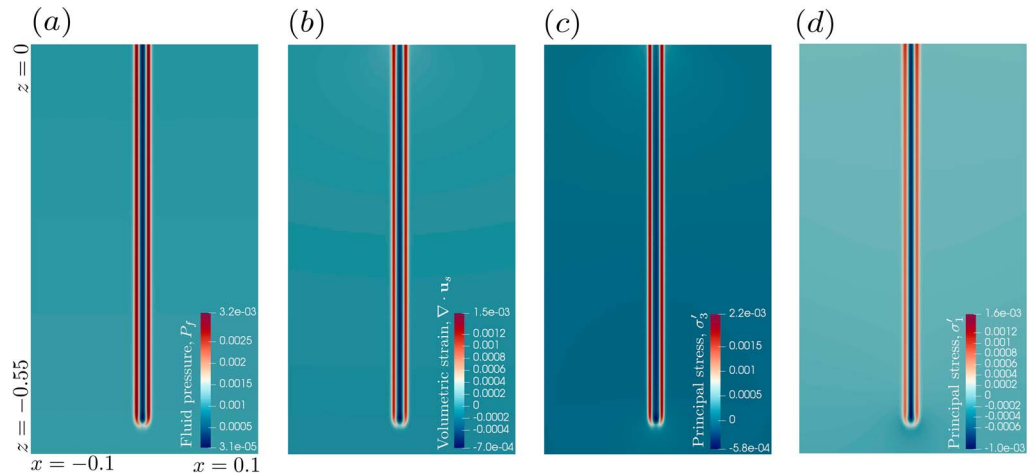


Figure 6. Model simulations with surface energy: $t = 0.5$ results for (a) fluid pressure P_f , (b) volumetric strain $\nabla \cdot \mathbf{u}_s$, (c) most tensile principal stress σ'_3 , and (d) most compressive principal stress σ'_1 . These were calculated with $w_0 = 10^{-7}$ m, $\mathcal{E} = 10^{-3}$, $K_\phi^c = 1$, $Da = 0.226$, and $\phi_0^c = 2\%$. The surface energy driven flow generates fluid overpressure (~ 32 MPa) and tensile stresses (~ 22 MPa) in a thin rim around the edge of the fracture zone.

open up mode I cracks parallel to the edge of the fracture zone. Furthermore, the stresses directly below the fracture zone will lead to cracks oriented perpendicular to the tip, suggesting that the initial fracture will migrate downward. Figure 7b shows the locations and orientations of the resulting tensile failure as a function of the uniaxial tensile strength T_u , where the pink dashes represent the mode I cracks that would form given the stress field at $t = 0.5$. For all tensile strengths in the range 5–20 MPa, the overpressured rim is cracked vertically down the entire length of the fracture zone. As T_u is decreased the cracks begin to form perpendicular to the leading edge of the tip.

Figure 8 shows the maximum tensile stress σ'_3 as a function of the initial fracture porosity ϕ_0^c for different \mathcal{E} . The fracture permeability factor in each case was chosen such that K_ϕ^c/Da is constant. For each \mathcal{E} we find that the tensile stress is an increasing function of the initial porosity. This is to be expected because a higher starting porosity implies a larger initial porosity gradient, and hence more surface energy driven fluid flow. Similarly, the tensile stresses are higher as \mathcal{E} is increased, as \mathcal{E} modulates the effective diffusivity of the surface energy term in equation (58). The maximum tensile stress ($\sigma'_3 \approx 55$ MPa) occurs when $\mathcal{E} = 10^{-2}$ and $\phi_0^c = 1$, and the dotted line indicates the 20 MPa threshold—anything exceeding this is likely to have failed in tension.

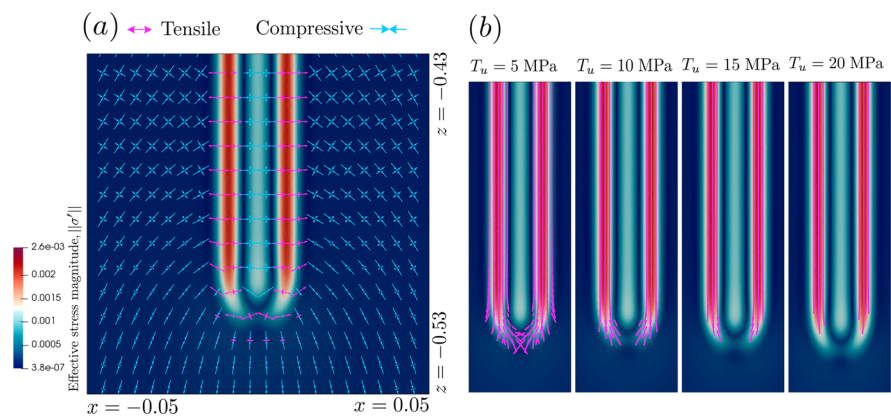


Figure 7. (a) Stress orientations with surface energy: $t = 0.5$ results for the principal axes around the tip of the fracture zone. The pink and blue arrows indicate tensile and compressive stresses, respectively. Each orthogonal pair of principal axes has been scaled similarly to Figure 3c, and the background shows the magnitude of the effective stress tensor (red is high, blue is low). Both panels indicate that the overpressured rim is in tension. (b) Tensile failure with surface energy: the pink dashes indicate the locations and orientations of mode I cracks that would open up for uniaxial tensile strengths of 5, 10, 15, and 20 MPa (going from left to right). All have been evaluated from the stress field at $t = 0.5$. The overpressured rim is lined with cracks aligned parallel to the perimeter of the fracture zone.

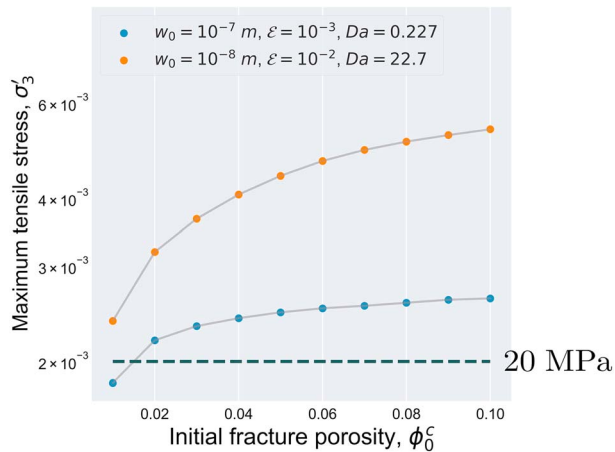


Figure 8. Both curves show the maximum value of the most tensile principal stress $\max(\sigma_3)$ as a function of the initial fracture porosity ϕ_0^c , corresponding to elastocapillary numbers of $\mathcal{E} = 10^{-2}$ (orange) and $\mathcal{E} = 10^{-3}$ (blue). The initial fracture porosity ϕ_0^c was varied linearly between 1 and 10%, and each point represents the solution evaluated at $t = 0.114/Da$. The dotted line shows the 20 MPa threshold.

7. Discussion

The model presented in this paper exhibits the type of self-limiting behavior that is described in section 1, that is, that the reaction results in a closure of pores due to fluid consumption and a reduction in permeability. Moreover, the reaction rate in equation (52) could also be extended to mimic the armoring of reactive surfaces by reaction products. In the absence of a process that creates new porosity, the model predicts that the phases are eventually exhausted, leaving behind a partially hydrated, impermeable rock. As discussed in section 6.2, the final degree of hydration is largely dependent on the amount of fluid that is present to start with, in addition to the ease with which the system can pull in additional fluid—either by pressure-driven or surface energy-driven flow—from external sources. Even for relatively high initial porosities ($\sim 10\%$) and enhanced permeability pathways connecting to a fluid source (represented by large K_ϕ^c in this model), the final degree of hydration will not exceed 30%. To reach 100% hydration, then, these results suggest that another mechanism is required.

The predicted stresses shown in Figure 3 indicate that the nonuniform volume changes in the vicinity of the fluid-rich fracture/fault lead to tensile failure. This lends support to the hypothesis that complete hydration could be facilitated by reaction-driven cracking. The mode of failure predicted in

this model is similar to observations of reaction-induced cracking in experiments involving olivine carbonation (Zhu et al., 2016), where it has been suggested that a mismatch in volume changes drives tensile failure. The predicted failure in Figure 4 indicates that mode I cracks will form perpendicular to the initial fracture, spanning from the tip up toward the seafloor boundary. Fracture textures similar to this, where a central vein is flanked by smaller, perpendicularly oriented veins (also known as *ladder cracks*) are observed in outcrops of altered peridotite. Figure 9 shows a typical example from Oman, alongside our numerical results (with the caveat that these outcrop textures also include the precipitation of carbonate minerals in veins). Additional cracks that open up at the seafloor (see Figures 4a–4c) would provide more sources of fluid and fast pathways for it to percolate down into the lithosphere. Moreover, the cracks that form around the tip of the fluid-rich region suggest that the initial fracture will migrate downward, in turn allowing fluid to access unreacted rock at greater depths.

Although this model demonstrates that reaction-driven volume changes can lead to failure, the behavior of the stresses and permeability is likely to change once the first crack has formed. Hence, the model in its current form cannot fully answer the critical question of whether reaction-driven cracking can lead to 100% hydration/carbonation, although it does suggest that initial reactive and surface energy driven stresses are

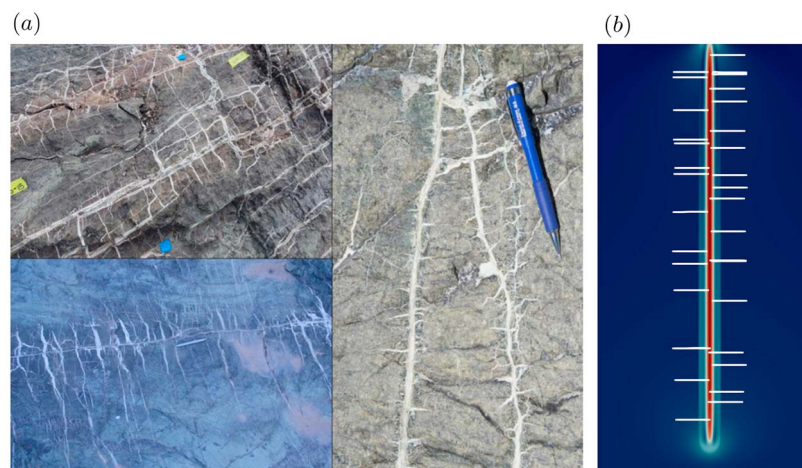


Figure 9. (a) Outcrops of partially serpentinized peridotite from Oman showing carbonate veins (in white) that exhibit orthogonal cross-cutting “ladder crack” textures. (b) A random sampling of predicted mode I cracks from a model simulation.

more than sufficient to drive brittle failure in an elastic medium. And, if it is possible, there is also the question of under what conditions, and what regions of parameter space, the system will allow the reaction to go to completion. In order to better understand the feedbacks in this process, it is clear that a model that couples fluid flow and failure is required. Nevertheless, given the added complexity (and potential ill-posedness) of brittle problems, we feel it is still useful to understand the possible consequences of hydration reactions, fluid flow, and surface energy in the better posed poroelastic regime first, and then investigate how failure modifies these solutions. It is also worth mentioning that, although full fluid saturation is a reasonable assumption in a subseafloor environment, it may be appropriate to consider a multiphase fluid model when the porosity is partially air-filled. Another setting that might lead to multiphase flow is if the fluid pressure reduces sufficiently for a vapor phase to form.

It is also worth noting that the inclusion of the eigenstrain in equation (16) posits the existence of a uniform volumetric strain that does not induce any additional stress. While this is a reasonable assumption in the case of uniform density changes, say, due to changes in equilibrium temperature, however, it is less clear how it should be implemented for a material where the reactions occur at grain/crack interfaces, where localized stresses should be generated at least at the grain scale. Experimental evidence (e.g., Zhu et al., 2016) in fact suggests that even homogeneous, unconfined reactions in water-olivine systems will lead to localized crack formation, which suggests that the introduction of an eigenstrain in this formulation probably underestimates the ability for reactions to produce brittle failure.

8. Conclusions

In this study we have derived a system of equations that describes the interaction of reactive fluids and solids in elastically deformable porous media, which in the absence of reaction reduces to standard Biot poroelasticity. These equations were applied to a two-dimensional model of serpentinization in a fractured/faulted subseafloor environment. We note that although serpentinization has been the focus of this study, these equations are general enough to extend to other types of reactions, for example, olivine carbonation. Furthermore, the reaction described by equation (1) can be modified to include dissolution of solid components into the fluid. Although the current formulation is dominantly mechanical, it could be made more general with the addition of an energy equation, which would in turn feedback into the reaction rates, densities, and potentially the surface energies.

Our numerical simulations demonstrate that, even for small initial fluid fractions, reaction-induced volume changes can lead to stresses in excess of the tensile strength of peridotite. We also found that increasing the overall fluid supply—either by enhancing the permeability or increasing the initial fluid fraction—leads to increased amounts of serpentinization and larger tensile stresses. When surface energy is significant the equations include an extra parameter that represents the relative importance of surface tension versus elastic forces. This parameter controls a diffusion-like term that drives fluid flow due to gradients in porosity. Our simulations showed that this term causes the system to swell around the fracture zone, resulting in large fluid overpressure/tensile stress. In addition to high-permeability pathways resulting from reaction-driven cracking, surface energy driven flow may be an important mechanism for allowing fluid to access regions of dry/unreacted rock.

Appendix A: Comparison With Biot's Theory of Poroelasticity

Here we clarify the equivalence between this model and Biot's equations of poroelasticity. First we derive the conservation equations of section 2 in the absence of reaction and surface energy, in addition to allowing for individually compressible solid grains. We then outline the derivation of Biot's equations under these same assumptions (following the description in (Verruijt, 2013) and show that these two formulations are equivalent.

In the absence of reaction we may rewrite the conservation of mass statements in equations (2)–(4) as

$$\frac{\partial}{\partial t} \rho_f \phi_f + \nabla \cdot \rho_f \phi_f \mathbf{v}_f = 0, \quad (\text{A1})$$

$$\frac{\partial}{\partial t} \rho_A \phi_A + \nabla \cdot \rho_A \phi_A \mathbf{v}_A = 0, \quad (\text{A2})$$

$$\frac{\partial}{\partial t} \rho_B \phi_B + \nabla \cdot \rho_B \phi_B \mathbf{v}_B = 0. \quad (\text{A3})$$

Adding equations (A2) and (A3) and using the constraint that $\rho_A \phi_A + \rho_B \phi_B = (1 - \phi) \rho_s$ yields a conservation of mass statement for the solid phase:

$$\frac{\partial \rho_s (1 - \phi)}{\partial t} + \nabla \cdot \rho_s (1 - \phi) \mathbf{v}_s = 0. \quad (\text{A4})$$

Using equations (A1) and (A4) leads to the following equation for the mean velocity $\bar{\mathbf{v}} \equiv \phi \mathbf{v}_f + (1 - \phi) \mathbf{v}_s$:

$$\nabla \cdot \bar{\mathbf{v}} = -\frac{\phi}{\rho_f} \frac{D_f \rho_f}{Dt} - \frac{1 - \phi}{\rho_s} \frac{D_s \rho_s}{Dt}. \quad (\text{A5})$$

Using fluid momentum equation (22) allows us to rewrite (A5) as

$$\nabla \cdot \mathbf{v}_s = -\nabla \cdot \mathbf{q} - \frac{\phi}{\rho_f} \frac{D_f \rho_f}{Dt} - \frac{1 - \phi}{\rho_s} \frac{D_s \rho_s}{Dt}, \quad (\text{A6})$$

where \mathbf{q} is the separation flux, which in the absence of surface tension is given by

$$\mathbf{q} = -\frac{\mathbf{K}_\phi}{\mu} [\nabla P_f - \rho_f \mathbf{g}]. \quad (\text{A7})$$

The assumption of small strains allows (A6) to be written as

$$\nabla \cdot \dot{\mathbf{u}}_s = -\nabla \cdot \mathbf{q} - \frac{\phi}{\rho_f} \frac{\partial \rho_f}{\partial t} - \frac{1 - \phi}{\rho_s} \frac{\partial \rho_s}{\partial t}. \quad (\text{A8})$$

We note that although the model derived in section 2 assumes that individual solid grains are incompressible, solid density changes are implicitly included in the reaction terms. In summary, equation (A8) is equivalent to (32) under the stated assumptions.

Biot (1941) states conservation of momentum for the solid (in the absence of body forces) in terms of the effective stress σ' as

$$\nabla \cdot \sigma' - \alpha \nabla P_f = 0, \quad (\text{A9})$$

where the effective stress is defined in terms of the total stress σ as

$$\sigma' = \sigma + \alpha P_f \mathbb{I}. \quad (\text{A10})$$

The Biot coefficient α describes how the bulk volume changes relative to the fluid pressure at a fixed stress, and is defined in Biot and Willis (1957) as

$$\alpha = 1 - C_s / C, \quad (\text{A11})$$

where C_s is the compressibility of solid particles and C is the compressibility of the porous medium. Equation (29) is equivalent to (A9) when the Biot coefficient $\alpha = 1$.

Conservation of mass is stated in Verruijt (2013) as

$$\alpha \nabla \cdot \dot{\mathbf{u}}_s + S \frac{\partial P_f}{\partial t} = -\nabla \cdot \mathbf{q}, \quad (\text{A12})$$

where \mathbf{u}_s is the solid displacement, S is the storativity and \mathbf{q} is the Darcy flux, which is given by

$$\mathbf{q} = -\frac{\mathbf{K}}{\mu} (\nabla P_f - \rho_f \mathbf{g}). \quad (\text{A13})$$

The storativity represents the relative fluid volume change per unit pressure change, and is defined as

$$S = \phi C_f + (\alpha - \phi) C_s, \quad (\text{A14})$$

where ϕ is the porosity and C_f is the fluid compressibility. We note that C_f is related to the fluid bulk modulus given in (28) by $C_f = 1/K_f$.

The isotropic component of the total stress $\hat{\sigma}$ can be written as

$$\hat{\sigma} = \hat{\sigma}' - \alpha P_f, \quad (\text{A15})$$

where $\hat{\sigma}' = \frac{1}{c} \nabla \cdot \mathbf{u}_s$. Substituting the above in (A12) yields

$$\nabla \cdot \mathbf{u}_s + \phi(C_f - C_s) \frac{\partial P_f}{\partial t} - C_s \frac{\partial \hat{\sigma}}{\partial t} = -\nabla \cdot \mathbf{q}. \quad (\text{A16})$$

Equations of state for the solid and fluid phases lead to the following constitutive relations:

$$\frac{\partial \rho_s}{\partial t} = \frac{\rho_s}{1 - \phi} \left[-C_s \frac{\partial \hat{\sigma}}{\partial t} - \phi C_f \frac{\partial P_f}{\partial t} \right], \quad (\text{A17})$$

$$\frac{\partial \rho_f}{\partial t} = C_f \rho_f \frac{\partial P_f}{\partial t}. \quad (\text{A18})$$

Finally, substituting these into (A16) yields

$$\nabla \cdot \mathbf{u}_s = -\nabla \cdot \mathbf{q} - \frac{\phi}{\rho_f} \frac{\partial \rho_f}{\partial t} - \frac{1 - \phi}{\rho_s} \frac{\partial \rho_s}{\partial t}, \quad (\text{A19})$$

which corresponds directly with (A8).

Appendix B: Numerical Solution Using Finite Elements

In section 6 we obtained numerical solutions to equations (55)–(58) using finite elements. This method leads to a solution of the weak form equations, where the solution is assumed to lie in a finite-dimensional subspace of piecewise continuous polynomials (of fixed degree) on a discretization of the domain. In this case the approximate solution $\mathbf{x} = (\phi, \phi_A, P_f, \mathbf{u}_s)$ is taken to lie in the function space $\mathcal{V} = [P_2 \times P_2 \times P_1 \times [P_2 \times P_2]]$. A projection of the effective stress tensor σ' can be recovered from the function space $\mathcal{V}_{\sigma'} = [[P_{1DG} \times P_{1DG}] \times [P_{1DG} \times P_{1DG}]]$, where P_{1DG} is the space of piecewise discontinuous linear functions.

As these equations are nonlinear, we must employ an iterative scheme that seeks to minimize the sum of the nonlinear residuals. The residuals for these equations are defined as follows:

$$F_{\mathbf{u}_s} = \int_{\Omega} \left[\epsilon_t : \sigma_i^k + \mathbf{u}_{st} \cdot \nabla P_{fi}^k - \frac{G\bar{\rho}}{\rho_f} (\mathbf{u}_{st} \cdot \hat{\mathbf{g}}) \right] dV, \quad (\text{B1})$$

$$F_{\phi} = \int_{\Omega} \left[\frac{\phi_t}{\Delta t} (\phi^k - \phi^{k-1} - (1 - [\phi]) \phi_i^k) \nabla \cdot [\mathbf{u}_{si}^k - \mathbf{u}_s^{k-1}] - \phi_t R_{\phi} \phi_i^k \phi_{Ai}^k \right] dV, \quad (\text{B2})$$

$$F_{\phi_A} = \int_{\Omega} \left[\frac{\phi_{At}}{\Delta t} (\phi_{Ai}^k - \phi_{Ai}^{k-1} + [\phi] \phi_{Ai}^k \nabla \cdot [\mathbf{u}_{si}^k - \mathbf{u}_s^{k-1}]) - \phi_{At} R_{\phi_A} \phi_i^k \phi_{Ai}^k \right] dV, \quad (\text{B3})$$

$$F_{P_f} = \int_{\Omega} \left[\frac{P_{ft}}{\Delta t} (\nabla \cdot [\mathbf{u}_{si}^k - \mathbf{u}_s^{k-1}] + \beta \phi_i^k [P_{fi}^k - P_f^{k-1}]) \right. \\ \left. + \nabla P_{ft} \cdot K_{\phi} [\nabla P_{fi}^k - G\hat{\mathbf{g}} + \mathcal{E}(\phi_i^k)^{-1/2} \nabla \phi_i^k] - P_{ft} R_{P_f} \phi_i^k \phi_{Ai}^k \right] dV. \quad (\text{B4})$$

where $\epsilon_t = \frac{1}{2}(\nabla \mathbf{u}_{st} + \mathbf{u}_{st}^T)$ is the symmetric gradient tensor of \mathbf{u}_{st} , $(\mathbf{u}_{st}^{k-1}, \phi^{k-1}, \phi_A^{k-1}, P_f^{k-1})$ are the solutions at the previous time step, $(\mathbf{u}_{si}^k, \phi_i^k, \phi_{Ai}^k, P_{fi}^k)$ are the solutions at the current time step and i th iteration, and $(\mathbf{u}_{st}, \phi_t, \phi_{At}, P_{ft})$ are the corresponding test functions. Here we have used a backward Euler method for the time integration.

The solution of the discrete weak problem at time step k is then equivalent to solving

$$F(\mathbf{x}^k) = \mathbf{0}, \quad (\text{B5})$$

where $F = F_{\mathbf{u}_s} + F_{\phi} + F_{\phi_A} + F_{P_f}$. To solve (B5) we use Newton's method with line search (as implemented in the PETSc SNES solver class), which obtains successive corrections to some approximation of the true solution. In other words, at each iteration we solve

$$F(\mathbf{x}_0^k + \delta\mathbf{x}^k) = \mathbf{0} \quad (\text{B6})$$

for the correction $\delta\mathbf{x}^k$, given an initial solution \mathbf{x}_0^k . Taylor expanding (B6) (and assuming that the correction is small) yields

$$\mathbf{J}(\mathbf{x}_0^k) \delta\mathbf{x}^k = -F(\mathbf{x}_0^k), \quad (\text{B7})$$

where \mathbf{J} is the Jacobian. At each iteration the linear problem (B7) is solved using a sparse direct solver (MUMPS; Amestoy et al., 2000, called through the PETSc interface), although all of the choices for nonlinear and linear solvers can be configured at run time through the TerraFERMA interfaces to PETSc. This whole procedure is repeated until some tolerance is met. All of the simulations in this study used TerraFERMA (Wilson et al., 2017) to leverage PETSc solvers (Balay et al., 2001) and libraries from the FEniCS project (Alnaes et al., 2015) for element choice, mesh management, and assembly.

Acknowledgments

The code used to generate these results can be found at the git repository https://github.com/orevans/poroelastic_serpenitization. We thank the Editor, two anonymous referees, and Richard Katz for constructive reviews that have significantly improved the quality of the manuscript. This work is supported by the National Science Foundation (grants EAR-1520732 and EAR-1516300). We acknowledge computing resources from Columbia University's Shared Research Computing Facility project, which is supported by NIH Research Facility Improvement grant 1G20RR030893-01, and associated funds from the New York State Empire State Development, Division of Science Technology and Innovation (NYSTAR) contract C090171, both awarded 15 April 2010. The authors thank the Isaac Newton Institute for Mathematical Sciences for its hospitality during the program Melt in the Mantle which was supported by EPSRC grant EP/K032208/1.

References

- Abramson, E. H., Brown, J. M., Slutsky, L. J., & Zaugg, J. (1997). The elastic constants of San Carlos olivine to 17 GPa. *Journal of Geophysical Research*, *102*, 12,253–12,264.
- Aharanov, E., Tenthorey, E., & Scholz, C. H. (1998). Precipitation sealing and diagenesis: 2. Theoretical analysis. *Journal of Geophysical Research*, *103*, 23,969–23,981.
- Alnaes, M. S., Blechta, J., Hake, J., Johansson, A., Kehlet, B., Logg, A., et al. (2015). The FEniCS project version 1.5. *Archive of Numerical Software*, *3*, 9–23.
- Amestoy, P. R., Duff, I. S., & L'Excellent, J. Y. (2000). Multifrontal parallel distributed symmetric and unsymmetric solvers. *Computer Methods in Applied Mechanics*, *184*, 501–520.
- Atkinson, B. K., & Avidis, V. (1980). Fracture mechanics parameters of some rock-forming minerals determined using an indentation technique. *International Journal of Rock Mechanics and Mining Sciences*, *17*, 383–386.
- Balay, S., Buschelman, K., Gropp, W. D., Kaushik, D., Knepley, M. G., McInnes, L. C., et al. (2001). PETSc web page.
- Barnes, I., & O'Neil, J. R. (1969). The relationship between fluids in some fresh alpine-type ultramafics and possible modern serpentinization, western United States. *Geological Society of America Bulletin*, *80*, 1947–1960.
- Barnes, I., O'Neil, J. R., & Trescases, J. J. (1978). Present day serpentinization in New Caledonia, Oman and Yugoslavia. *Geochimica et Cosmochimica Acta*, *42*, 144–145.
- Bercovici, D., & Ricard, Y. (2003). Energetics of a two-phase model of lithospheric damage, shear localization and plate-boundary formation. *Geophysical Journal International*, *152*, 581–596.
- Bercovici, D., Ricard, Y., & Schubert, G. (2001a). A two-phase model for compaction and damage: 1. General theory. *Journal of Geophysical Research*, *106*, 8887–8906.
- Bercovici, D., Ricard, Y., & Schubert, G. (2001b). A two-phase model for compaction and damage: 3. Applications to shear localization and plate boundary formation. *Journal of Geophysical Research*, *106*, 8925–8939.
- Bertrand, T., Peixinho, J., Mukhopadhyay, S., & MacMinn, C. W. (2016). Dynamics of swelling and drying in a spherical gel. *Physical Review Applied*, *6*, 064010.
- Biot, M. A. (1941). General theory of three-dimensional consolidation. *Journal of Applied Physics*, *12*, 155–164.
- Biot, M. A., & Willis, D. G. (1957). The elastic coefficients of the theory of consolidation. *Journal of Applied Mechanics*, *24*, 594–601.
- Bruni, J., Canepa, M., Chiodini, G., Cioni, R., Cipolli, F., Longinelli, A., et al. (2002). Irreversible water-rock mass transfer accompanying the generation of the neutral, Mg-HCO₃ and high-pH, Ca-OH spring waters of the Genova province, Italy. *Applied Geochemistry*, *17*, 455–474.
- Cai, M. (2010). Practical estimates of tensile strength and Hoek-Brown strength parameter m_i of brittle rocks. *Rock Mechanics and Rock Engineering*, *42*, 167–184.
- Chavagnac, V., Ceuleneer, G., Monnin, C., Lansac, B., Hoareau, G., & Boulart, C. (2013). Mineralogical assemblages forming at hyperalkaline warm springs hosted on ultramafic rocks: A case study of Oman and Ligurian ophiolites. *Geochemistry Geophysics Geosystems*, *14*, 2474–2495.
- Chavagnac, V., Monnin, C., Ceuleneer, G., Boulart, C., & Hoareau, G. (2013). Characterization of hyperalkaline fluids produced by low-temperature serpentinization of mantle peridotites in the Oman and Ligurian ophiolites. *Geochemistry Geophysics Geosystems*, *14*, 2496–2522.
- Coleman, R. G., & Keith, T. E. (1971). A chemical study of serpentinization—Burro Mountain, California. *Journal of Petrology*, *12*, 311–328.
- Craft, K. L., & Lowell, R. P. (2009). A boundary layer model for submarine hydrothermal heat flows at on-axis and near-axis regions. *Geochemistry Geophysics Geosystems*, *10*, Q12012. <https://doi.org/10.1029/2009GC002707>
- De Groot, S. R., & Mazur, P. (1962). *Non-equilibrium thermodynamics*. New York: North-Holland, Amsterdam; Wiley.
- Dewandel, B., Lachassagne, P., Boudier, F., Al-Hattali, S., Ladouche, B., Pinault, J. L., & Al-Suleimani, Z. (2005). A conceptual hydrogeological model of ophiolite hard-rock aquifers in Oman based on a multiscale and a multidisciplinary approach. *Hydrogeology Journal*, *13*, 708–726.
- Drew, D. A., & Segel, L. A. (1971). Averaged equations for two-phase flows. *Studies in Applied Mathematics*, *50*, 205–231.
- Faccenda, M. (2014). Water in the slab: A trilogy. *Tectonophysics*, *614*, 1–30.
- Falk, E. S., & Kelemen, P. B. (2015). Geochemistry and petrology of listvenite in the Samail ophiolite, Sultanate of Oman: Complete carbonation of peridotite during ophiolite emplacement. *Geochimica et Cosmochimica Acta*, *160*, 70–90.

- Fletcher, R. C., Buss, H. L., & Brantley, S. L. (2006). A spheroidal weathering model coupling porewater chemistry to soil thicknesses during steady-state denudation. *Earth and Planetary Science Letters*, *244*, 444–457.
- Fletcher, R. C., & Merino, E. (2001). Mineral growth in rocks: Kinetic-rheological models of replacement, vein formation, and syntectonic crystallization. *Geochimica et Cosmochimica Acta*, *65*, 3733–3748.
- Fowler, A. (1985). A mathematical model of magma transport in the asthenosphere. *Geophysical & Astrophysical Fluid*, *33*, 63–96.
- Gorman, P. J., Kerrick, D. M., & Connolly, J. D. (2006). Modeling open system metamorphic decarbonation of subducting slabs. *Geochemistry Geophysics Geosystems*, *4*, Q04007. <https://doi.org/10.1029/2005GC00112>
- Gueguen, Y., & Dienes, J. (1989). Transport properties of rocks from statistics and percolation. *Mathematical Geosciences*, *21*, 1–13.
- Hadley, K. (1976). Comparison of calculated and observed crack densities and seismic velocities in westerly granite. *Journal of Geophysical Research*, *81*, 3484–3494.
- Hier-Majumder, S., Ricard, Y., & Bercovici, D. (2006). Role of grain boundaries in magma migration and storage. *Earth and Planetary Science Letters*, *248*, 735–749.
- Iyer, K., Jamtveit, B., Mathiesen, J., Malthe-Sørenssen, A., & Feder, J. (2008). Reaction-assisted hierarchical fracturing during serpentinization. *Earth and Planetary Science Letters*, *267*, 503–516.
- Jamtveit, B., Kobchenko, M., Austrheim, H., Malthe-Sørenssen, A., Røyne, A., & Svensen, H. (2011). Porosity evolution and crystallization-driven fragmentation during weathering of andesite. *Journal of Geophysical Research*, *116*, B12204. <https://doi.org/10.1029/2011JB008649>
- Jamtveit, B., Malthe-Sørenssen, A., & Kostenko, O. (2008). Reaction enhanced permeability during retrogressive metamorphism. *Earth and Planetary Science Letters*, *276*, 620–627.
- Katz, R. F. (2008). Magma dynamics with the enthalpy method: Benchmark solutions and magmatic focusing at mid-ocean ridges. *Journal of Petrology*, *49*, 2099–2121.
- Katz, R. F., Spiegelman, M., & Holtzman, B. (2006). The dynamics of melt and shear localization in partially molten aggregates. *Nature*, *442*, 676.
- Kelemen, P. B., Godard, M., Johnson, K. T. M., Okazaki, K., Manning, C. E., Urai, J. L., et al. the Oman Drilling Project Phase I Science Team (2017). Peridotite carbonation at the leading edge of the mantle wedge: OmDP site BT1. AGU Fall Meeting 2017.
- Kelemen, P. B., & Hirth, G. (2012). Reaction-driven cracking during retrograde metamorphism: Olivine hydration and carbonation. *Earth and Planetary Science Letters*, *345*, 81–89.
- Kelemen, P. B., & Matter, J. (2008). In situ carbonation of peridotite for CO₂ storage. *Proceedings of the National Academy of Sciences of the United States of America*, *105*, 17,295–17,300.
- Kelemen, P. B., Matter, J., Streit, E. E., Rudge, J. F., Curry, W. B., & Blusztajn, J. (2011). Rates and mechanisms of mineral carbonation in peridotite: Natural processes and recipes for enhanced, in situ CO₂ capture and storage. *Earth and Planetary Science Letters*, *39*, 545–576.
- Keller, T., May, D. A., & Kaus, B. J. P. (2013). Numerical modelling of magma dynamics coupled to tectonic deformation of lithosphere and crust. *Geophysical Journal International*, *195*, 1406–1442.
- Kelley, D. S., Karson, J. A., Früh-Green, G. L., Yoerger, D. R., Shank, T. M., Butterfield, D. A., et al. (2005). A serpentinite-hosted ecosystem: The Lost City hydrothermal field. *Science*, *307*, 1428–1434.
- Kirby, S., Engdahl, R. E., & Denlinger, R. (1996). Intermediate-depth intraslab earthquakes and arc volcanism as physical expressions of crustal and uppermost mantle metamorphism in subducting slabs. *Subduction Geophysical Monograph Series*, *96*, 195–214.
- Lafay, R., Montes-Hernandez, G., Janots, E., Chiriac, R., Findling, N., & Toche, F. (2012). Mineral replacement rate of olivine by chrysotile and brucite under high alkaline conditions. *Journal of Crystal Growth*, *347*, 62–72.
- Lamadrid, H. M., Rimstidt, J. D., Schwarzenbach, E. M., Klein, F., Ulrich, S., Dolocan, A., & Bodnar, R. J. (2017). Effect of water activity on rates of serpentinization of olivine. *Nature Communications*, *8*, 16107.
- MacMinn, C. W., Dufresne, E. R., & Wettlaufer, J. S. (2016). Large deformations of a soft porous material. *Physical Review Applied*, *5*, 044020.
- Macdonald, A. H., & Fyfe, W. S. (1985). Rate of serpentinization in seafloor environments. *Tectonophysics*, *116*, 123–135.
- Malvoisin, B., Brantut, N., & Kaczmarek, M. A. (2017). Control of serpentinisation rate by reaction-induced cracking. *Earth and Planetary Science Letters*, *476*, 143–152.
- Malvoisin, B., Brunet, F., Carlut, J., Rouméjon, S., & Cannat, M. (2012). Serpentinization of oceanic peridotites: 2. Kinetics and processes of San Carlos olivine hydrothermal alteration. *Journal of Geophysical Research*, *117*, B04102. <https://doi.org/10.1029/2011JB008842>
- Manning, C. E., & Ingebritsen, S. E. (1999). Permeability of the continental crust: Implications of geothermal data and metamorphic systems. *Reviews of Geophysics*, *37*, 127–150.
- Martin, B., & Fyfe, W. S. (1970). Some experimental and theoretical observations on the kinetics of hydration reactions with particular reference to serpentinization. *Chemical Geology*, *6*, 185–202.
- McCollom, T. M., Klein, F., Robbins, M., Moskowitz, B., Berquó, T. S., Jöns, N., et al. (2016). Temperature trends for reaction rates, hydrogen generation, and partitioning of iron during experimental serpentinization of olivine. *Geochimica et Cosmochimica Acta*, *181*, 175–200.
- McKenzie, D. (1984). The generation and compaction of partially molten rock. *Journal of Petrology*, *25*, 713–765.
- Mervine, E. M., Humphris, S. E., Sims, K. W., Kelemen, P. B., Kelemen, & Jenkins, W. J. (2013). Carbonation rates of peridotite in the Samail Ophiolite, Sultanate of Oman, constrained through ¹⁴C dating and stable isotopes. *Geochimica et Cosmochimica Acta*, *126*, 371–397.
- Mura, T. (1987). General theory of eigenstrains, *Micromechanics of Defects in Solids* (pp. 1–73). Dordrecht, Netherlands: Springer.
- Ogasawara, Y., Okamoto, A., Hirano, N., & Tsuchiya, N. (2013). Coupled reactions and silica diffusion during serpentinization. *Geochimica et Cosmochimica Acta*, *119*, 212–230.
- Parks, G. A. (1984). Surface and interfacial free energies of quartz. *Journal of Geophysical Research*, *89*, 3997–4008.
- Paterson, M. S. (1978). *Experimental rock deformation: The brittle field*. New York: Springer-Verlag.
- Plümpner, O., Røyne, A., Magrasó, A., & Jamtveit, B. (2012). The interface-scale mechanism of reaction-induced fracturing during serpentinization. *Geology*, *40*, 1103–1106.
- Prigogine, I. (1967). *Introduction to thermodynamics of irreversible processes*. New York: Wiley-Interscience.
- Ranero, C. R., Morgan, J. P., McIntosh, K., & Reichert, C. (2003). Bending-related faulting and mantle serpentinization at the Middle America trench. *Nature*, *425*, 367–373.
- Riley, G. N., & Kohlstedt, D. L. (1991). Kinetics of melt migration in upper mantle-type rocks. *Earth and Planetary Science Letters*, *105*, 500–521.
- Roland, E., Behn, M. D., & Hirth, G. (2010). Thermal–mechanical behavior of oceanic transform faults: Implications for the spatial distribution of seismicity. *Geochemistry Geophysics Geosystems*, *11*, Q07001. <https://doi.org/10.1029/2010GC003034>
- Rudge, J. F., Bercovici, D., & Spiegelman, M. (2011). Disequilibrium melting of a two phase multicomponent mantle. *Geophysical Journal International*, *184*, 699–718.

- Rudge, J. F., Kelemen, P. B., & Spiegelman, M. (2010). A simple model of reaction-induced cracking applied to serpentinization and carbonation of peridotite. *Earth and Planetary Science Letters*, *291*, 215–227.
- Scholz, C. H. (2002). *The mechanics of earthquakes and faulting*. Cambridge, UK: Cambridge University Press.
- Scott, D. R., & Stevenson, D. J. (1986). Magma ascent by porous flow. *Journal of Geophysical Research*, *91*, 9283–9296.
- Scott, D. R., & Stevenson, D. J. (1989). A self-consistent model of melting, magma migration and buoyancy-driven circulation beneath mid-ocean ridges. *Journal of Geophysical Research*, *94*, 2973–2988.
- Seyfried, W. E., Pester, N. J., Tutolo, B. M., & Ding, K. (2015). The Lost City hydrothermal system: Constraints imposed by vent fluid chemistry and reaction path models on seafloor heat and mass transfer processes. *Geochimica et Cosmochimica Acta*, *163*, 59–79.
- Simpson, G., Spiegelman, M., & Weinstein, M. I. (2010a). A multiscale model of partial melts: 1. Effective equations. *Journal of Geophysical Research*, *115*, B04410. <https://doi.org/10.1029/2009JB006375>
- Simpson, G., Spiegelman, M., & Weinstein, M. I. (2010b). A multiscale model of partial melts: 2. Numerical results. *Journal of Geophysical Research*, *115*, B04411. <https://doi.org/10.1029/2009JB006376>
- Spiegelman, M. (1993a). Flow in deformable porous media. Part 1. Simple analysis. *Journal of Fluid Mechanics*, *247*, 17–38.
- Spiegelman, M. (1993b). Flow in deformable porous media. Part 2. Numerical analysis—The relationship between shock waves and solitary waves. *Journal of Fluid Mechanics*, *247*, 39–63.
- Spiegelman, M., Kelemen, P. B., & Aharonov, E. (2001). Causes and consequences of flow organization during melt transport: the reaction infiltration instability in compactible media. *Journal of Geophysical Research*, *106*, 2061–2077. <https://doi.org/10.1029/2000JB900240>
- Stevenson, D. J. (1986). On the role of surface-tension in the migration of melts and fluids. *Geophysical Research Letters*, *13*, 1149–1152.
- Tapponnier, P., & Brace, W. F. (1976). Development of stress-induced microcracks in westerly granite. *International Journal of Rock Mechanics and Mining Sciences*, *13*, 103–112.
- Tenthorey, E., Scholz, C. H., Aharonov, E., & Léger, A. (1998). Precipitation sealing and diagenesis: 1. Experimental results. *Journal of Geophysical Research*, *103*, 23,951–23,967.
- Timoshenko, S. P., & Goodier, J. N. (1970). *Theory of elasticity*. New York: McGraw-Hill.
- Ulven, O. I., Jamtveit, B., & Malthe-Sørenssen, A. (2014). Reaction-driven fracturing of porous rock. *Journal of Geophysical Research: Solid Earth*, *119*, 7473–7486. <https://doi.org/10.1002/2014JB011102>
- Ulven, O. I., Storheim, H., Austrheim, H., & Malthe-Sørenssen, A. (2014). Fracture initiation during volume increasing reactions in rocks and applications for CO₂ sequestration. *Earth and Planetary Science Letters*, *389*, 132–142.
- van Keken, P. E., Hacker, B. R., Syracuse, E. M., & Abers, G. A. (2011). Subduction factory: 4. Depth-dependent flux of H₂O from subducting slabs worldwide. *Journal of Geophysical Research*, *116*, B01401. <https://doi.org/10.1029/2010JB007922>
- Vermilye, J. M., & Scholz, C. H. (1995). Relation between vein length and aperture. *Journal of Structural Geology*, *17*, 423–434.
- Verruijt, A. (2013). Theory and problems of poroelasticity (Technical report). Delft University of Technology.
- Wegner, W. W., & Ernst, W. G. (1983). Experimentally determined hydration and dehydration reaction rates in the system MgO-SiO₂-H₂O. *American Journal of Science*, *283*, 151–180.
- Wilson, C. R., Spiegelman, M., & van Keken, P. E. (2017). TerraFERMA: The transparent finite element rapid model assembler for multiphysics problems in Earth sciences. *Geochemistry Geophysics Geosystems*, *18*, 769–810. <https://doi.org/10.1002/2016GC006702>
- Wilson, C. R., Spiegelman, M., van Keken, P. E., & Hacker, B. R. (2014). Fluid flow in subduction zones: The role of solid rheology and compaction pressure. *Earth and Planetary Science Letters*, *401*, 261–274.
- Wu, Y. S., Zhang, K., & Liu, H. H. (2006). Estimating large-scale fracture permeability of unsaturated rock using barometric pressure data. *Vadose Zone Journal*, *5*, 1129–1142.
- Zhu, W., Fusses, F., Lisabeth, H., Xing, T., Xiao, X., De Andrade, V., & Karato, S. I. (2016). Experimental evidence of reaction-induced fracturing during olivine carbonation. *Geophysical Research Letters*, *43*, 9535–9543. <https://doi.org/10.1002/2016GL070834>